Constraints on dark matter to dark radiation conversion in the late universe with DES-Y1 and external data

A. Chen,[1,*] D. Huterer,[1] S. Lee,[2] A. Ferté,[3] N. Weaverdyck,[1] O. Alves,[4] C. D. Leonard,[5] N. MacCrann,[6,7] M. Raveri,[8] A. Porredon,[6,9,10] E. Di Valentino,[11] J. Muir,[12] P. Lemos,[13] A. R. Liddle,[14,15,16] J. Blazek,[6,17] A. Campos,[18,4] R. Cawthon,[19] A. Choi,[6] S. Dodelson,[18] J. Elvin-Poole,[6,7] D. Gruen,[20,12,21] A. J. Ross,[6] L. F. Secco,[22] I. Sevilla-Noarbe,[23] E. Sheldon,[24] M. A. Troxel,[2] J. Zuntz,[15] T. M. C. Abbott,[25] M. Aguena,[26,27] S. Allam,[28] J. Annis,[28] S. Avila,[29] E. Bertin,[30,31] S. Bhargava,[32] S. L. Bridle,[11] D. Brooks,[13] A. Carnero Rosell,[33,34] M. Carrasco Kind,[35,36] J. Carretero,[37] M. Costanzi,[38,39] M. Crocce,[9,10] L. N. da Costa,[27,40] M. E. S. Pereira,[1] T. M. Davis,[41] P. Doel,[13] T. F. Eifler,[42,3] I. Ferrero,[43] P. Fosalba,[9,10] J. Frieman,[28,8] J. García-Bellido,[29] E. Gaztanaga,[9,10] D. W. Gerdes,[44,1] R. A. Gruendl,[35,36] J. Gschwend,[27,40] G. Gutierrez,[28] S. R. Hinton,[41] D. L. Hollowood,[45] K. Honscheid,[6,7] B. Hoyle,[46,47,48] D. J. James,[49] M. Jarvis,[22] K. Kuehn,[50,51] O. Lahav,[13] M. A. G. Maia,[27,40] J. L. Marshall,[52] F. Menanteau,[35,36] R. Miquel,[53,37] R. Morgan,[19] A. Palmese,[28,8] F. Paz-Chinchón,[54,36] A. A. Plazas,[55] A. Roodman,[12,21] E. Sanchez,[23] V. Scarpine,[28] M. Schubnell,[1] S. Serrano,[9,10] M. Smith,[56] E. Suchyta,[57] G. Tarle,[1] D. Thomas,[58] C. To,[20,12,21] T. N. Varga,[47,48] J. Weller,[47,48] and R. D. Wilkinson[32]

(DES Collaboration)

[1]*Department of Physics, University of Michigan, Ann Arbor, Michigan 48109, USA*
[2]*Department of Physics, Duke University Durham, North Carolina 27708, USA*
[3]*Jet Propulsion Laboratory, California Institute of Technology, 4800 Oak Grove Drive, Pasadena, California 91109, USA*
[4]*Instituto de Física Teórica, Universidade Estadual Paulista, São Paulo, Brazil*
[5]*School of Mathematics, Statistics and Physics, Newcastle Unviersity, NE1 7RU, United Kingdom*
[6]*Center for Cosmology and Astro-Particle Physics, The Ohio State University, Columbus, Ohio 43210, USA*
[7]*Department of Physics, The Ohio State University, Columbus, Ohio 43210, USA*
[8]*Kavli Institute for Cosmological Physics, University of Chicago, Chicago, Illinois 60637, USA*
[9]*Institut d'Estudis Espacials de Catalunya (IEEC), Barcelona 08034, Spain*
[10]*Institute of Space Sciences (ICE, CSIC), Campus UAB, Carrer de Can Magrans, s/n, Barcelona 08193, Spain*
[11]*Jodrell Bank Center for Astrophysics, School of Physics and Astronomy, University of Manchester, Oxford Road, Manchester, M13 9PL, United Kingdom*
[12]*Kavli Institute for Particle Astrophysics & Cosmology, P. O. Box 2450, Stanford University, Stanford, California 94305, USA*
[13]*Department of Physics & Astronomy, University College London, Gower Street, London, WC1E 6BT, United Kingdom*
[14]*Instituto de Astrofísica e Ciências do Espaço, Faculdade de Ciências, Universidade de Lisboa, 1769-016 Lisboa, Portugal*
[15]*Institute for Astronomy, University of Edinburgh, Edinburgh EH9 3HJ, United Kingdom*
[16]*Perimeter Institute for Theoretical Physics, 31 Caroline Street North, Waterloo, Ontario N2L 2Y5, Canada*
[17]*Institute of Physics, Laboratory of Astrophysics, École Polytechnique Fédérale de Lausanne (EPFL), Observatoire de Sauverny, 1290 Versoix, Switzerland*
[18]*Department of Physics, Carnegie Mellon University, Pittsburgh, Pennsylvania 15312, USA*
[19]*Physics Department, 2320 Chamberlin Hall, University of Wisconsin-Madison, 1150 University Avenue Madison, Wisconsin 53706-1390, USA*
[20]*Department of Physics, Stanford University, 382 Via Pueblo Mall, Stanford, California 94305, USA*
[21]*SLAC National Accelerator Laboratory, Menlo Park, California 94025, USA*
[22]*Department of Physics and Astronomy, University of Pennsylvania, Philadelphia, Pennsylvania 19104, USA*
[23]*Centro de Investigaciones Energéticas, Medioambientales y Tecnológicas (CIEMAT), Madrid, Spain*
[24]*Brookhaven National Laboratory, Building 510, Upton, New York 11973, USA*
[25]*Cerro Tololo Inter-American Observatory, NSF's National Optical-Infrared Astronomy Research Laboratory, Casilla 603, La Serena, Chile*
[26]*Departamento de Física Matemática, Instituto de Física, Universidade de São Paulo, CP 66318, São Paulo, SP, 05314-970, Brazil*

2470-0010/2021/103(12)/123528(25)

[27]Laboratório Interinstitucional de e-Astronomia—LIneA, Rua Gal. José Cristino 77, Rio de Janeiro, RJ 20921-400, Brazil
[28]Fermi National Accelerator Laboratory, P. O. Box 500, Batavia, Illinois 60510, USA
[29]Instituto de Fisica Teorica UAM/CSIC, Universidad Autonoma de Madrid, 28049 Madrid, Spain
[30]CNRS, UMR 7095, Institut d'Astrophysique de Paris, F-75014, Paris, France
[31]Sorbonne Universités, UPMC Univ Paris 06, UMR 7095, Institut d'Astrophysique de Paris, F-75014, Paris, France
[32]Department of Physics and Astronomy, Pevensey Building, University of Sussex, Brighton BN1 9QH, United Kingdom
[33]Instituto de Astrofisica de Canarias, E-38205 La Laguna, Tenerife, Spain
[34]Universidad de La Laguna, Dpto. Astrofísica, E-38206 La Laguna, Tenerife, Spain
[35]Department of Astronomy, University of Illinois at Urbana-Champaign, 1002 W. Green Street, Urbana, Illinois 61801, USA
[36]National Center for Supercomputing Applications, 1205 West Clark Street, Urbana, Illinois 61801, USA
[37]Institut de Física d'Altes Energies (IFAE), The Barcelona Institute of Science and Technology, Campus UAB, 08193 Bellaterra (Barcelona) Spain
[38]INAF-Osservatorio Astronomico di Trieste, via G. B. Tiepolo 11, I-34143 Trieste, Italy
[39]Institute for Fundamental Physics of the Universe, Via Beirut 2, 34014 Trieste, Italy
[40]Observatório Nacional, Rua Gal. José Cristino 77, Rio de Janeiro, RJ 20921-400, Brazil
[41]School of Mathematics and Physics, University of Queensland, Brisbane, QLD 4072, Australia
[42]Department of Astronomy/Steward Observatory, University of Arizona, 933 North Cherry Avenue, Tucson, Arizona 85721-0065, USA
[43]Institute of Theoretical Astrophysics, University of Oslo. P.O. Box 1029 Blindern, NO-0315 Oslo, Norway
[44]Department of Astronomy, University of Michigan, Ann Arbor, Michigan 48109, USA
[45]Santa Cruz Institute for Particle Physics, Santa Cruz, California 95064, USA
[46]Faculty of Physics, Ludwig-Maximilians-Universität, Scheinerstr. 1, 81679 Munich, Germany
[47]Max Planck Institute for Extraterrestrial Physics, Giessenbachstrasse, 85748 Garching, Germany
[48]Universitäts-Sternwarte, Fakultät für Physik, Ludwig-Maximilians Universität München, Scheinerstr. 1, 81679 München, Germany
[49]Center for Astrophysics | Harvard & Smithsonian, 60 Garden Street, Cambridge, Massachusetts 02138, USA
[50]Australian Astronomical Optics, Macquarie University, North Ryde, NSW 2113, Australia
[51]Lowell Observatory, 1400 Mars Hill Road, Flagstaff, Arizona 86001, USA
[52]George P. and Cynthia Woods Mitchell Institute for Fundamental Physics and Astronomy, and Department of Physics and Astronomy, Texas A&M University, College Station, Texas 77843, USA
[53]Institució Catalana de Recerca i Estudis Avançats, E-08010 Barcelona, Spain
[54]Institute of Astronomy, University of Cambridge, Madingley Road, Cambridge CB3 0HA, United Kingdom
[55]Department of Astrophysical Sciences, Princeton University, Peyton Hall, Princeton, New Jersey 08544, USA
[56]School of Physics and Astronomy, University of Southampton, Southampton, SO17 1BJ, United Kingdom
[57]Computer Science and Mathematics Division, Oak Ridge National Laboratory, Oak Ridge, Tennessee 37831, USA
[58]Institute of Cosmology and Gravitation, University of Portsmouth, Portsmouth PO1 3FX, United Kingdom

(Received 18 November 2020; accepted 29 April 2021; published 10 June 2021)

We study a phenomenological class of models where dark matter converts to dark radiation in the low redshift epoch. This class of models, dubbed DMDR, characterizes the evolution of comoving dark-matter density with two extra parameters, and may be able to help alleviate the observed discrepancies between early and late-time probes of the Universe. We investigate how the conversion affects key cosmological observables such as the cosmic microwave background (CMB) temperature and matter power spectra. Combining 3x2pt data from Year 1 of the Dark Energy Survey, *Planck*-2018 CMB temperature and polarization data, supernovae (SN) Type Ia data from Pantheon, and baryon acoustic oscillation (BAO) data from BOSS DR12, MGS and 6dFGS, we place new constraints on the amount of dark matter that has

*Corresponding author:
anqich@umich.edu

converted to dark radiation and the rate of this conversion. The fraction of the dark matter that has converted since the beginning of the Universe in units of the current amount of dark matter, ζ, is constrained at 68% confidence level to be <0.32 for DES-Y1 3x2pt data, < 0.030 for CMB + SN + BAO data, and <0.037 for the combined dataset. The probability that the DES and CMB+SN+BAO datasets are concordant increases from 4% for the ΛCDM model to 8% (less tension) for DMDR. The tension in $S_8 = \sigma_8\sqrt{\Omega_m/0.3}$ between DES-Y1 3x2pt and CMB + SN + BAO is slightly reduced from 2.3σ to 1.9σ. We find no reduction in the Hubble tension when the combined data is compared to distance-ladder measurements in the DMDR model. The maximum-posterior goodness-of-fit statistics of DMDR and ΛCDM model are comparable, indicating no preference for the DMDR cosmology over ΛCDM.

DOI: 10.1103/PhysRevD.103.123528

I. INTRODUCTION

Over the past few years, there has been a notable improvement in both the variety and precision of cosmological probes. Signals predicted long ago, such as gravitational waves and global 21-cm absorption, were finally observed, providing new insights and solidifying our understanding of the Universe. The enhanced precision of relatively mature observational techniques such as measurements of galaxy clustering, weak lensing, and anisotropies in the cosmic microwave background (CMB) temperature and polarization fields has allowed us to test the ΛCDM paradigm to an unprecedented degree.

Recent cosmological observations have revealed a discrepancy in the inferred Hubble constant at $\gtrsim 4\sigma$ level between early and late Universe probes [1–3]. With a strengthening of the various steps in the local distance-ladder measurements of H_0, as well as tightening constraints of medium-to-high redshift probes such as strong and weak gravitational lensing, the Hubble tension is becoming more significant [4–7] and enormous effort has been devoted to understanding its origin. A number of theories have thus far been proposed to help ameliorate or resolve the tension [8–18], but so far none have done so to a satisfactory degree.

A parallel development over the last few years has been the consistently lower value of the amplitude of mass fluctuations σ_8 measured in gravitational lensing compared to that measured by the CMB experiments [19–24]. While not currently statistically as strong as the Hubble tension, the persistence of the σ_8 measurement discrepancies, as well as their possible origin as a mismatch between the geometrical measures and the growth of structure expected in the currently dominant ΛCDM paradigm, deserves special attention. It would be very exciting, and compelling, if both the H_0 and σ_8 tensions were solved simultaneously, though the success of extant models on this front is at best mixed [25–30].

One possible explanation for why weak lensing surveys measure a smaller amplitude of fluctuations than the CMB is that the present-day matter content has decreased at a higher rate than predicted by ΛCDM model. Models where dark matter converts into a new species with radiation properties that is not directly detectable (hence "dark radiation") can enable such a trend. These models also have the potential to reconcile the Hubble tension, as they predict a smaller matter content as time evolves. Accordingly, dark energy dominates faster than in ΛCDM in these models, giving a larger late-time acceleration rate (indicated by a higher H_0). Therefore, decaying or annihilating dark-matter models, such as those studied previously in Refs. [31–48], offer a tantalizing hope of resolving the H_0 and σ_8 tensions simultaneously.

In this paper, we are specifically interested in the class of models where the energy density in dark matter monotonically converts into dark radiation, with the bulk of the activity happening at low redshift (late time). Our motivation is to investigate whether a model where dark matter converts to dark radiation—henceforth, a DMDR model—can satisfy the twin requirements of both being favored by the data and helping alleviate the Hubble and σ_8 tensions.

In general, interacting dark-matter models have the potential to resolve the observations in cosmology that might be otherwise difficult to explain in the standard ΛCDM model. Because models with beyond-cold-dark-matter particle content often wash out small-scale structure [49,50], they are well positioned to help alleviate the well-documented challenges observed on small scales (the core/cusp, missing satellites and too-big-to-fail problems of CDM [51]). The integrated Sachs-Wolfe (ISW) effect has been measured to have an amplitude significantly higher than that predicted in ΛCDM when stacking large voids in the large-scale structure [52,53]; the decrease of dark matter would suppress the Weyl potential on large scales, thus enhancing the ISW effect and could thus help to explain this. Finally, cosmic rays from unidentified sources, specifically the galactic positron excess at ~300 GeV [54] and the ~3.5 keV [55] x-ray line from nearby galaxies, have been hypothesized to be sourced by the decay of dark matter [56–60] (although they may be inconsistent with some specific dark-matter particle models [61,62]). All of these lines of inquiry motivate further study of the properties of, and constraints on, the classes of models with

DMDR conversion. For example, Wang et al. [56,63] investigated a decaying dark-matter model that could be mapped into the parameter space of the phenomenological DMDR conversion scenario studied in this paper, and showed that their model can mitigate some of the aforementioned small-scale CDM challenges.

On the theory side, dark-matter-dark-radiation conversion is predicted in various physically motivated scenarios [39,64,65]. In particle-dark-matter theories, an unstable dark-matter component is predicted in various extensions of the Standard Model. For example, in nonminimal supersymmetric models, the dark sector has a spectrum of particles analogous to particles in the Standard Model, and heavier particles can decay into the lightest supersymmetric particle [66] which could have properties of dark radiation [67]. More generally, beyond-Standard-Model physics including fifth-force type additional interactions, can naturally accommodate dark-matter and dark-radiation couplings. Some have proposed such coupled models as a mechanism to solve the 21-cm absorption anomaly seen by the EDGES experiment [68,69]. Furthermore, inspiraling and colliding primordial black holes (PBHs)—dark-matter candidates in their own right [70]—could transfer energy from dark matter to gravitational waves, which are also a form of dark radiation [42,71]. PBHs could also evaporate into beyond-standard-model relativistic species through Hawking radiation [72]. Various constraints on PBH abundance were extensively studied by the dynamical, lensing, evaporation, and accretion footprints of the PBHs [70,73], but several mass windows remain unconstrained, and previously closed windows sometimes reopen when revisited with improved analysis tools [74–76].

Any of the aforementioned theoretical models could underlie a phenomenological dark-matter-dark-radiation conversion model. The key signature of such a model, compared to the standard ΛCDM model, is the decreased fraction of dark matter in favor of both dark radiation and dark energy.

Our goal is to study a phenomenological cosmological DMDR model using state-of-the-art cosmological observations. In this work we utilize the CMB temperature, polarization, and lensing potential angular power spectra measured by Planck [1], together with type Ia supernovae from Pantheon [77], baryon acoustic oscillations (BAO) from the BOSS [78], MGS [79], and 6dFGS [80] surveys, and tomographic galaxy clustering and weak lensing measured by the Dark Energy Survey (DES) [22].

This work is presented as follows. We introduce our DMDR model in Sec. II, stressing its signatures in the CMB and matter power spectrum. In Sec. III, we present the details of our analysis pipeline, including the datasets we use and the theoretical predictions of the DMDR model. In Sec. IV, we report combined constraints on the DMDR model from DES-Y1 and external data, along with model comparison between DMDR and ΛCDM. We conclude in Sec. V.

II. THE DMDR MODEL

Our specific implementation of the dark-matter-dark-radiation conversion model is based on the phenomenological model studied by Bringmann et al. [42], hereafter B18. We focus on the case where the conversion process accelerates in time, and the major departures from ΛCDM happen at late times, as shown in Fig. 1. To obtain a phenomenological model with this behavior, we impose an additional boundary condition onto the original B18 three-parameter ansatz to obtain a steeper rate of dark-matter conversion in the recent past ($z \lesssim 10$); see the next subsection. Overall, our DMDR model introduces two additional parameterscompared to ΛCDM.

We now describe the background equations for the model, followed by the description of its perturbations.

A. Background equations

The background evolution of the DMDR model is specified by the ansatz of the decreasing dark-matter density and the modified continuity equation

$$\rho_{\rm dm}(a) = \frac{\rho^0_{\rm dm}}{a^3}\left[1 + \zeta\frac{1 - a^\kappa}{1 + \zeta a^\kappa}\right], \tag{1}$$

$$\frac{1}{a^3}\frac{d}{dt}(a^3\rho_{\rm dm}) = -\frac{1}{a^4}\frac{d}{dt}(a^4\rho_{\rm dr}) = -Q, \tag{2}$$

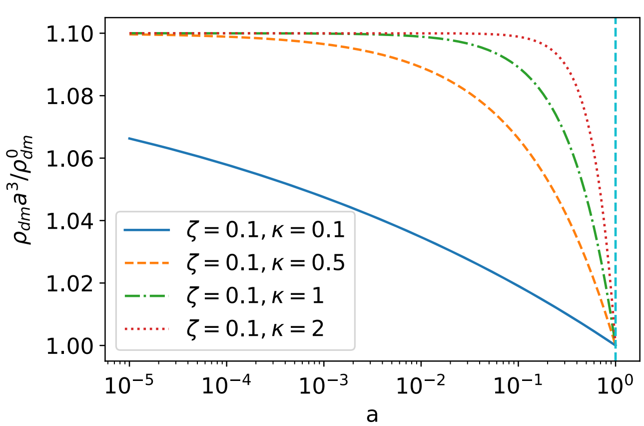

FIG. 1. Temporal evolution of the comoving dark-matter density (in units of current dark-matter density $\rho^0_{\rm DM}$. The legend shows the assumed values of ζ, the fraction of dark matter that has converted into dark radiation since the early Universe relative to current density, and κ, the conversion rate of dark matter. We fixed the standard cosmological parameters to their fiducial values as reported in Sec. II A.

where $\rho_{\rm dm}$ and $\rho_{\rm dr}$ are dark-matter and dark-radiation energy densities, $\rho^0_{\rm dm}$ is the dark-matter density today, a is the scale factor, and we introduce two new parameters[1]:

(1) ζ, the total amount of dark matter that has already converted into dark radiation, divided by the amount of dark matter at the current time.

(2) κ, the parameter characterizing the conversion rate. The duration of the conversion roughly corresponds to $O(1/\kappa)$ orders of magnitude change in the scale factor.

Equation (1) provides an ansatz for the time evolution of the comoving density of dark matter. In our late-time DMDR conversion model, the bulk of the conversion occurs around the present time ($a \simeq 1$). Equation (2) specifies that the energy transfers from dark matter to dark radiation. It also determines the energy transfer flux, $\mathcal{Q}$, as a function of the scale factor a, taking the derivative of equation (1).

Like the original B18 model, our DMDR model has the generality to cover a wide class of decaying/annihilating dark-matter model. For most of the popular decaying/annihilating dark-matter models with smooth and simple transition curve, in the $a < 1$ region a specific value of κ that numerically mimic the transition curve of the dark-matter density can be found. Note, since the condition of accelerating conversion rate in the near past is similar to pushing the transition time (labeled by the maximum dark-matter conversion rate) to the future, in the single-body decaying dark-matter scenario it suggests a very small decay rate, $\Gamma \ll H_0^{-1}$.

To illustrate the evolution of background quantities, we first discuss the fiducial cosmological model. We fix the non-DMDR cosmological parameters to the following values based on DES-Y1 fiducial values: matter and baryon densities relative to critical $\Omega_m = 0.3028$ and $\Omega_b = 0.04793$, scaled Hubble constant $h = 0.6818$, spectral index and amplitude of primordial density fluctuations $n_s = 0.9694$ and $A_s = 2.198 \times 10^{-9}$, physical neutrino density $\Omega_\nu h^2 = 0.0006155$ (corresponding to the sum of the neutrino masses of 0.058 eV), and optical depth to reionization $\tau = 0.06972$. These parameters, which are common to both DMDR and ΛCDM models, are also adopted in the illustrations and Fisher forecasts throughout the following sections. We stress that the values of the standard cosmological parameters such as h and Ω_m are by definition set at the present time. Thus the high-z region of the DMDR models in these figures has higher dark-matter density. The detailed effect of the DMDR parameters ζ and κ is illustrated in the first batch of figures in this paper, which we now describe.

[1]The original ansatz in B18 has three parameters: ζ, κ, a_t, where the last parameter is the characteristic scale factor when the conversion happened. Here we set the mathematical condition $\rho_{\rm dm} a^3 = 0$ as $a \to \infty$ to obtain an accelerated decreasing curve near $a = 1$. This condition leads to an identity among the three parameters, $1 - \zeta a_t^\kappa = 0$. We then substitute $a_t = \exp(-\log(\zeta)/\kappa)$ back into the B18 ansatz, arriving at our Eq. (1) which contains the remaining parameters ζ and κ. Keeping ζ or a_t in our model is equivalent; we opted for ζ based on the fact that it is the more physically intuitive parameter in this case.

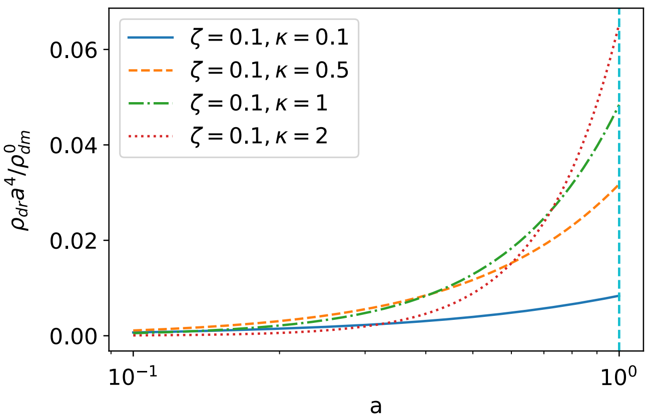

FIG. 2. Same as Fig. 1, but now showing the temporal evolution of the dark *radiation* density.

Figure 1 shows how the density of dark matter evolves with scale factor, relative to ΛCDM, for different conversion rates. Varying ζ scales the curves up and down; in the illustrative plots that follow we choose $\zeta = 0.1$. We show the matter density evolution for four different values of the conversion rate κ; results in Fig. 1 and subsequent figures shows rapid changes in the dark-matter density in $a \gtrsim 0.1$, suggesting that we may be able to place constraints on such models using current LSS observations.

Figure 2 shows how the density of dark radiation evolves with scale factor for different conversion rates, relative to ΛCDM. As the conversion rate parameter κ increases, the density of dark radiation in the late Universe increases faster. When the dark radiation is produced in the nearer past (for higher κ), it dilutes less than if produced over a longer span of time (lower κ); thus there is more dark radiation at $a = 1$ in a larger-κ Universe. One may worry that large-κ models may be automatically ruled out because they apparently lead to a high number of effective relativistic species $\Delta N_{\rm eff} = \rho_{\rm dr}/\rho_\nu$, but note that the conversion to dark radiation happens at very low redshifts in our DMDR model and thus renders a simple comparison with $\Delta N_{\rm eff}$ constraints derived from the CMB impossible. Hence a detailed analysis of the combination of CMB, LSS, and geometric probes is necessary. A more direct impact of dark radiation will be on the expansion history, however, and this will be constrained by the supernova data in our analysis. For the hypergeometric function required to calculate the background density of the dark radiation, we used the special function routine from Ref. [81].

Figure 3 shows how the Hubble expansion rate evolves with scale factor for different conversion rates, relative to ΛCDM. Note that we implicitly hold the present-day values of Ω_m and h constant in this plot. Then, increasing the

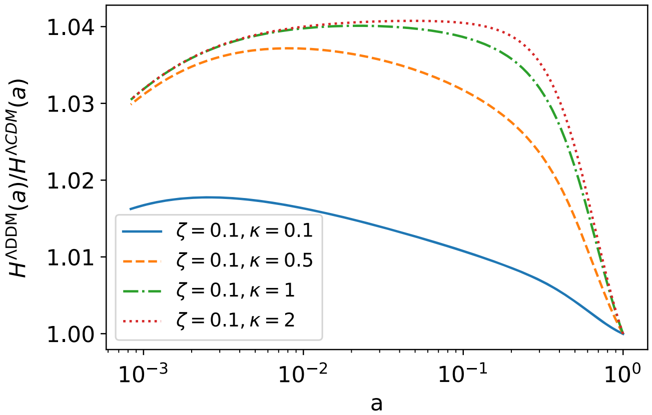

FIG. 3. Same as Fig. 1, but now showing time evolution in the ratio between DMDR and ΛCDM Hubble parameter.

conversion rate of dark matter κ *increases* the amount of dark matter at $a < 1$ relative to today, and hence leads to a more rapid expansion rate, so that $H^{\mathrm{DMDR}}(a)/H^{\mathrm{LCDM}}(a) > 1$ as seen in Fig. 3.

B. Perturbation equations

In order to get the matter and radiation perturbation power spectra, we next need to write down the linear perturbation equations of motion for both dark matter and dark radiation, then implement them in the Boltzmann numerical solver CAMB [82]. We adopt the synchronous gauge throughout this section, following the convention of CAMB. The metric perturbation in synchronous gauge is [83]

$$ds^2 = a^2(\tau)[-d\tau^2 + (\delta_{ij} + h_{ij})dx^i dx^j], \tag{3}$$

where τ is the comoving time, and h_{ij} with $i, j = 1, 2, 3$ is the metric perturbation.

Most often, dark radiation is treated as a new species of massless neutrinos (e.g., [42,84]). This conjecture works fine in the scenario with no massive neutrinos, but it produces an incorrect matter power spectrum that evolves discontinuously away from ΛCDM when *massive* neutrinos are present. Such behavior is expected because dark radiation (unlike the massless neutrinos) does not interact with massive neutrinos nor does it share the same temperature and entropy with them. In CAMB, the distribution of the energy between neutrino species are specified by a set of time-independent degeneracy numbers, but this is not applicable to the model with energy transfer from dark matter to dark radiation.[2] Therefore, as long as the model does not allow for dark matter to massless neutrino conversion, the two species are physically distinct and treating dark radiation as a new type of a massless neutrino is incorrect. Thus we choose to treat dark radiation as an independent perturbation component in the Boltzmann equations.

In our model, we assume the dark matter to always be cold, meaning that the conversion process to the dark radiation does not provide enough recoil kinetic energy to heat up the dark matter. At the same time, dark radiation in our model does not self-interact or dissipate energy via interactions with dark matter, standard-model particles, or photons after their production, so that dark radiation simply free streams. As a result, the phase-space perturbation equations for the dark radiation differ from the massless-neutrino ones only by a collision term. Adopting the perturbation-expansion notation from [83], we have

$$dN = f(x^i, P_j, \tau)dx^1 dx^2 dx^3 dP_1 dP_2 dP_3, \tag{4}$$

$$f(x^i, P_j, \tau) = f_0(q)[1 + \Psi(x^i, q, n_j, \tau)], \tag{5}$$

$$F(\vec{k}, \hat{n}, \tau) = \frac{\int q^2 dq q f_0(q)\Psi(\vec{k}, q, \hat{n}, \tau)}{\int q^2 dq q f_0(q)}, \tag{6}$$

where x^i are comoving coordinates, P_i are their conjugate momentum, and dN is the particle number in the phase space differential volume. Here the momentum variable P_i is replaced by q and n_i variables through $P_i = (\delta_{ij} + \frac{1}{2}h_{ij})qn_j$ in the second equation, and k space is Fourier transformed from x space.

The dark radiation phase-space equation of motion reads

$$\frac{\partial F_{\mathrm{dr}}(\vec{k}, \hat{n}, \tau)}{\partial \tau} + ik\mu F_{\mathrm{dr}}(\vec{k}, \hat{n}, \tau) = -\frac{2}{3}\dot{h}(\vec{k}, \tau) - \frac{4}{3}(\dot{h}(\vec{k}, \tau) + 6\dot{\eta}(\vec{k}, \tau))P_2(\hat{k}\cdot\hat{n}) + \left(\frac{\partial F_{\mathrm{dr}}(\vec{k}, \hat{n}, \tau)}{\partial \tau}\right)_C, \tag{7}$$

where $(\partial F_{\mathrm{dr}}(\vec{k}, \hat{n}, \tau)/\partial\tau)_C$ is the additional collision term due to the conversion between dark matter and dark radiation, to be contrasted with the collisionless massless neutrino equations.

We adopt a simple form for the collision perturbation equation involving no dependence on polarization or momentum anisotropy. Specifically,

$$\left(\frac{\partial F_{\mathrm{dr}}(\vec{k}, \hat{n}, \tau)}{\partial \tau}\right)_C = \frac{\mathcal{Q}(a)a}{\rho_{\mathrm{dr}}(a)}(-F_{\mathrm{dr}}(\vec{k}, \hat{n}, \tau) + \delta_{\mathrm{dm}}(\vec{k}, \tau)), \tag{8}$$

where $\mathcal{Q}$ is defined in equation (2). When writing down Eq. (8), we adopted the minimal form for the perturbation variation of the conversion term $\mathcal{Q}$:

[2] In the all-massless neutrino case the problem of incorrect time-independent degeneracy numbers could be hidden, because there is no need to partition the energy for the massless species sharing the same equation of motion.

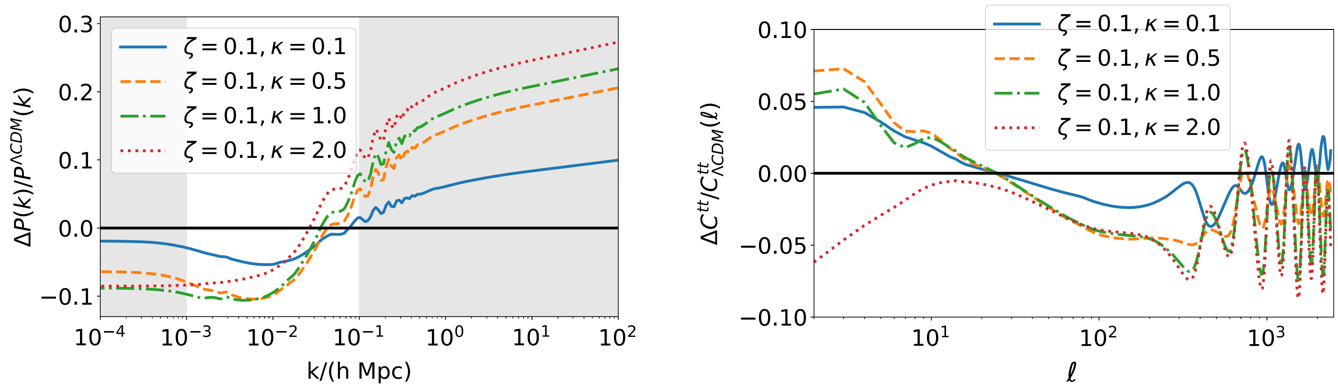

FIG. 4. Relative difference in the matter power spectrum (left panel) and CMB TT spectrum (right panel) between DMDR and ΛCDM. We explore the same four sets of (ζ, κ) values as in the previous three figures. In the left panel, the white region (between the two shaded regions) denotes roughly the scales used by the DES 3x2pt analysis.

$$\delta\mathcal{Q} = \mathcal{Q}\delta_{\rm dm}. \tag{9}$$

In principle, the form of $\delta\mathcal{Q}$ is determined by the microphysics of the dark-matter-dark-radiation conversion process. The minimal form above has been adopted by previous literature [40,41,85], and B18 has demonstrated that the current generation cosmology observations do not have high enough precision to distinguish the detailed $\delta\mathcal{Q}$ perturbation by carrying out case studies on Sommerfeld enhancement and single-body decay process.

After harmonic expansion of Eq. (7), we get the hierarchy equations for dark radiation. Along with the dark-matter perturbation equations, the full set of perturbation equations in DMDR model reads [83,84,86,87]:

$$\delta'_{\rm dm} + k\mathcal{Z} = \frac{a}{\bar{\rho}_{\rm dm}}(\mathcal{Q}\delta_{\rm dm} - \delta\mathcal{Q}) = 0, \qquad \text{[Dark Matter]}, \tag{10}$$

$$\delta'_{\rm dr} = -\frac{4}{3}k\mathcal{Z} - kq_{\rm dr} - \frac{a\mathcal{Q}}{\bar{\rho}_{\rm dr}}(\delta_{\rm dr} - \delta_{\rm dm}), \qquad \text{[Dark Radiation}, \ell = 0], \tag{11}$$

$$q'_{\rm dr} = \frac{k}{3}\delta_{\rm dr} - \frac{2}{3}k\beta_2\pi_{\rm dr} - \frac{a\mathcal{Q}}{\bar{\rho}_{\rm dr}}q_{\rm dr}, \qquad \text{[Dark Radiation}, \ell = 1], \tag{12}$$

$$\pi'_{\rm dr} = \frac{2}{5}kq_{\rm dr} - \frac{3}{5}k\beta_3 J_3^{\rm dr} + \frac{8}{15}k\sigma - \frac{a\mathcal{Q}}{\bar{\rho}_{\rm dr}}\pi_{\rm dr}, \qquad \text{[Dark Radiation}, \ell = 2], \tag{13}$$

$$J_\ell^{\rm dr\prime} = \frac{k}{2\ell+1}[\ell J_{\ell-1}^{\rm dr} - \beta_{\ell+1}(\ell+1)J_{\ell+1}^{\rm dr}] - \frac{a\mathcal{Q}}{\bar{\rho}_{\rm dr}}J_\ell^{\rm dr}, \qquad \text{[Dark Radiation}, \ell > 2], \tag{14}$$

where J_ℓ are the harmonic expansions of the phase space perturbation, $J_0^{\rm dr} \equiv \delta_{\rm dr}$, $J_1^{\rm dr} \equiv q_{\rm dr} = \frac{4}{3}\theta_{\rm dr}/k$, $J_2^{\rm dr} \equiv \pi_{\rm dr} = \Pi^{\rm dr}/\bar{\rho}_{\rm dr}$ in CAMB convention; $\mathcal{Z}$ and σ are the metric perturbation coefficients, and β_ℓ are the harmonic expansion coefficients of the gradient operator defined in Ref. [84]. Further details of this derivation are included in Appendix B.

The modifications described above are relevant for the continuity equations. For the Einstein equations, the correction is rather straightforward: we simply add the dark-radiation perturbations to the total energy-momentum perturbations.

C. CMB and matter power spectrum

We now have the ingredients necessary to numerically compute the CMB polarized temperature anisotropies and matter perturbation power spectra, and thus derive the observable quantities that can be compared to data. We implement the background and perturbation equations in the previous two subsections in the Einstein-Boltzmann code

CAMB [82] which is used in the cosmosis pipeline that we discuss in more detail below.[3]

Figure 4 illustrates the relative differences between the DMDR and ΛCDM matter power spectra and their CMB spectra. As with the background-evolution illustrations above, we fix the parameters common to both DMDR and ΛCDM model to their fiducial values listed in Sec. II A, and we only vary DMDR-specific parameters ζ and κ. This ensures that the two cosmologies always converge at late times (see also Fig. 1). In the early Universe, DMDR has more dark matter than ΛCDM, and this makes the matter and CMB power spectra resemble those in a ΛCDM cosmology but with more dark matter. This, in turn, shows up as the small-scale power enhancement, as well as the phase shift in the case of the CMB power spectrum.

A distinctive feature in DMDR is the dip in the matter power spectrum at $k \sim 10^{-2}\ h\,\mathrm{Mpc}^{-1}$, the scale corresponding to the horizon crossing at matter-radiation equality. This feature is mostly due to the different expansion history in a higher dark-matter density universe in DMDR. Although we see an increase in the matter power around $k \sim 0.1\ h/\mathrm{Mpc}$, and might worry that it could boost the amplitude of mass fluctuations σ_8 and thus exacerbate the LSS tension with CMB, note that this is not the case because we have artificially held most of the cosmological parameters fixed. In fact, DMDR can be qualitatively compared and contrasted with the early dark energy models [9,28]. While the early dark energy models have a larger dark-matter-to-dark-energy ratio after recombination than ΛCDM, the DMDR model have a *smaller* such ratio relative to ΛCDM. This works in the direction of reconciling the σ_8 tension.

In the CMB temperature power spectrum shown on the right in Fig. 4, the decreasing dark-matter density leads to an increase in the late ISW effect caused by the decrease of the gravitational potential as dark matter converts into dark radiation (an exception is the $\kappa = 2$ case which we discuss separately below). Late-ISW effect is caused by the decrease of Weyl potential in the dark-energy-dominant epoch as the expansion of Universe accelerates. In ΛCDM, the decrease of the Weyl potential only happens in the dark-energy-dominated epoch while the potential remains constant in dark-matter epoch, but in the DMDR model the late-ISW effect also accumulates in the dark-matter-dominated epoch. This is because the Weyl potential is mainly contributed to by dark matter and a decreasing comoving density of dark matter leads to a decreasing Weyl potential even before dark energy takes over. Although DMDR imprints in the late-ISW effect are probably buried in the cosmic variance, it does gives these models an additional signature that can be sought in e.g., studies of the ISW imprints in the large voids [53].

[3]DMDR-CAMB using the background and perturbation equations in this work can be found here: https://bitbucket.org/anqich/ddm-camb/src/master/. Please email the corresponding author to get access if it is needed.

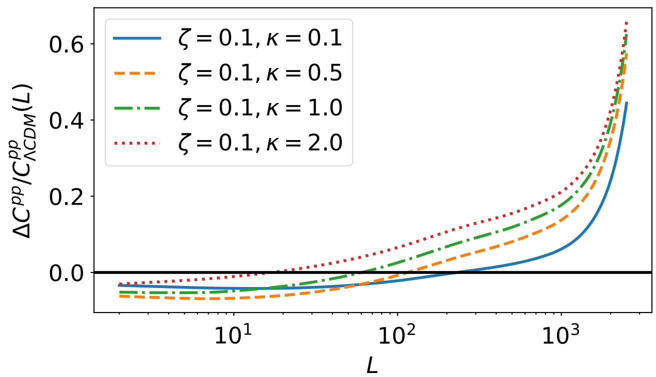

FIG. 5. Relative difference in the CMB lensing potential spectrum between DMDR and ΛCDM, as a function of κ for $\zeta = 0.1$.

The red curve in Fig. 4 requires further discussion. This is the case where the dark matter converts at very late times ($z \simeq O(1)$) and rapidly. Therefore, the increased dark-energy-to-dark-matter ratio that is characteristic of DMDR model occurs too late for the late-time ISW to fully benefit from it. In addition, a DMDR model with the same present-day Ω_m as a ΛCDM model has more matter relative to dark energy at $z > 0$; therefore, contributions to late-time ISW occur later in DMDR than in ΛCDM. These two effects combine to severely suppress the late-time ISW effect in high-κ DMDR models.

Lastly, we also present the DMDR effect on the lensing potential power spectrum for CMB; see Fig. 5. We observe an increase of the lensing potential at small scales (large multipoles L) that mimics the amplified large k modes of matter power spectrum seen in Fig. 4.

D. Nonlinear matter power spectrum strategies and DES-Y1 scales used

Obtaining accurate theoretical predictions for nonlinear clustering in cosmological models outside of ΛCDM is typically challenging, as these predictions require running suites of cosmological simulations designed specifically for the extended models. This situation can be contrasted to that in ΛCDM (and its simplest extension that assume a free but constant dark energy equation of state, wCDM), where the modeling of nonlinear matter power spectrum has been extensively studied with N-body simulations [88–90] and analytical fits or models [91–94]. Limited previous studies of the small-scale structure formation in DMDR include simulations of a less general class of decaying dark-matter models than the one we adopt here [40], and the demonstration that relativistic species have negligible contribution to the gravitational physics of the small-scale structure formation [95]. One potentially useful alternative to running simulations is recent work [96] which proposes to accurately model beyond-ΛCDM models by suitably rescaling the ΛCDM result in order to get one into the desired new model. These results are potentially useful and we may study and implement some of them in the future, but they are currently not validated to the level sufficient to enable us to model the nonlinear clustering in our DMDR cosmological model.

We therefore choose to limit our analysis to purely linear scales, thus following the same strategy as in the DES-Y1 modified gravity analysis [97] (see also Ref. [98]). To summarize, we start with the difference between the nonlinear and linear-theory predictions of the observed data in the standard ΛCDM model at best-fit values of cosmological parameters, $\mathbf{d}_{\rm NL} - \mathbf{d}_{\rm lin}$. Using also the full error covariance of DES-Y1, $\mathbf{C}$, we calculate the quantity

$$\Delta\chi^2 \equiv (\mathbf{d}_{\rm NL} - \mathbf{d}_{\rm lin})^T \mathbf{C}^{-1} (\mathbf{d}_{\rm NL} - \mathbf{d}_{\rm lin}) \tag{15}$$

and identify the single data point that contributes most to this quantity. We remove that data point, and repeat the process masking out $\mathbf{d}_{\rm NL} < \mathbf{d}_{\rm lin}$ region until $\Delta\chi^2 < 1$. The resulting set of 334 (compared to the DES-Y1 3x2pt baseline 457) data points that remain constitutes our fiducial choice of linear-only scales.

E. Expectations and forecasts

Before analyzing the data, we perform a forecast of the expected constraints. We do so in order to understand the parameter degeneracy structure, especially in regards to the new parameters ζ and κ. We would also like to understand what constraints are expected on these parameters. However, not all the likelihoods we plan to use in the real-data analysis have the corresponding mock likelihoods available. So for the forecast, we only use the DES-Y1 3x2pt and the Planck-2018 TT-TE-EE-lite data centered at the fiducial ΛCDM cosmology. The likelihood of simulated Planck data vector was calculated by implementing a wrapper of the work of Ref. [99] in COSMOSIS.

To obtain the forecasts on parameter constraints, we adopt the Fisher matrix methodology. The Fisher matrix is defined as

$$\mathcal{F}_{ij} = \sum_{mn} \frac{\partial v_m}{\partial p_i} [C^{-1}]_{mn} \frac{\partial v_n}{\partial p_j} + [\mathcal{I}^{-1}]_{ij} \tag{16}$$

evaluated at the fiducial cosmology, where v_m are the theoretically predicted data values, p_i are the cosmological and nuisance parameters, C_{ij} is the covariance matrix of the data, and $\mathcal{I}_{ij}$ is the covariance matrix of parameter priors. Fisher matrix calculations typically incorporate Gaussian priors on the parameters. Because we have flat priors on some of our parameters (see Table I), we adopt Gaussian priors of which the *variance* scales with the range (hence variance) of the flat priors that we have. Such Gaussian prior approximations are illustrated by black lines in Fig. 6.

TABLE I. Cosmological and nuisance parameters in DES-Y1 3x2pt analysis and their priors.

Parameter	Prior
Cosmological	
Ω_m	Flat (0.1, 0.9)
h	Flat (0.55, 0.91)
Ω_b	Flat (0.03, 0.07)
n_s	Flat (0.87, 1.07)
A_s	Flat $(5 \times 10^{-10}, 5 \times 10^{-9})$
$\Omega_\nu h_0^2$	Flat (0.0006, 0.01)
ζ	FLAT (0.0, 1.0)
κ	flat $(1 \times 10^{-7}, 2.0)$
σ_8 (derived)	$\in$ (0.4, 1.4)
Lens galaxy bias	
$b_i, (i = 1, \ldots 5)$	Flat (0.8, 3.0)
Intrinsic alignment	
$A_{IA}(z) = A_{IA}[(1+z)/1.62]\eta_{IA}$	
A_{IA}	Flat $(-5, 5)$
η_{IA}	Flat $(-5, 5)$
Lens photo-z shift (red sequence)	
Δz_l^1	Gauss (0.008, 0.007)
Δz_l^2	Gauss $(-0.005, 0.007)$
Δz_l^3	Gauss (0.006, 0.006)
Δz_l^4	Gauss (0.00, 0.01)
Δz_l^5	Gauss (0.00, 0.01)
Source photo-z shift	
Δz_s^1	Gauss $(-0.001, 0.016)$
Δz_s^2	Gauss $(-0.019, 0.013)$
Δz_s^3	Gauss (0.009, 0.011)
Δz_s^4	Gauss $(-0.018, 0.022)$
Shear calibration	
$m^i, (i = 1, \ldots 4)$	Gauss (0.012, 0.023)

Thus we add $\mathcal{I}_{ij} = \delta_{ij}{\rm Var}[\mathcal{P}(p_i)]$, where δ_{ij} is the Kronecker Delta and $\mathcal{P}(p_i)$ is any one of the Gaussian approximation of the flat priors from Table I. We center the cosmological parameters at the values listed in Sec. II A. For the near-fiducial ΛCDM Fisher calculation, we adopt the DMDR parameter values of $\zeta = 10^{-4}$ and $\kappa = 1.0$, where all the cosmological observables have negligible difference from ΛCDM due to small ζ yet is sensitive enough to the two additional parameters. We use the COSMOSIS[4] [100] Fisher sampler to forecast the constraints on the DMDR parameters.

In the Fisher forecast results shown in Fig. 6, we observe that

(i) The DMDR model breaks the tight correlation between Ω_m and h for *Planck*. In ΛCDM Ω_m and h are strongly anticorrelated because $\Omega_m h^2$ is tightly constrained by the morphology of the acoustic peaks in the CMB spectrum. In DMDR, the background evolution has more freedom given by the variation of

[4]https://bitbucket.org/joezuntz/cosmosis/wiki/Home.

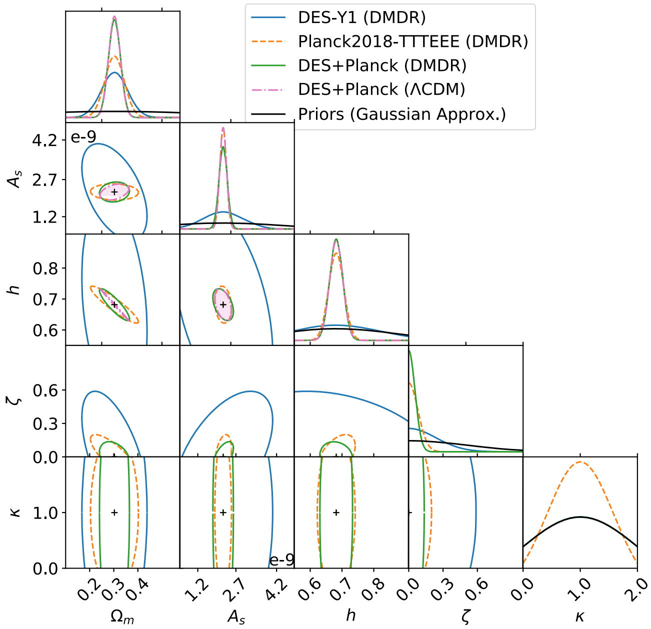

FIG. 6. The DMDR Fisher forecasts showing 95% C.L. contours assuming simulated DES-Y1 3x2pt data, simulated *Planck*-2018 data, and the combination of both, all generated close to ΛCDM cosmology. The forecast is done assuming a Gaussian surface around the fiducial ΛCDM cosmology, specified by the same parameters in Sec. II A. The combined datasets noticeably increased the constraint power, especially on the fraction of converted dark matter ζ. The ΛCDM model's degeneracy between h and Ω_m (note a very thin red contour in that plane) opened up in DMDR.

ζ and κ, thus weakening this degeneracy by adding more degrees of freedom in this 2D space.

(ii) Furthermore, DES has a different degeneracy direction from Planck in the $\Omega_m - h$ plane, so that when the two probes are combined the degeneracy in this space is significantly reduced. Because ζ is significantly correlated with Ω_m, this degeneracy breaking greatly helps in constraining ζ.

(iii) In Fig. 6 we assumed a DMDR cosmology very close to ΛCDM (with $\zeta = 10^{-4}$). In that case, there is effectively no constraint on the conversion rate κ, as expected.

Note again that the Fisher forecasts above are centered at $\zeta = 10^{-4}$, $\kappa = 1.0$ (near) ΛCDM. We have checked that, as the fiducial values of both ζ and κ increase away from their ΛCDM values of zero, the forecasted constraints strengthen. Such behavior in Fisher matrix forecasts is not uncommon and occurs when the dependence of the measured quantities on the parameters of interest is nonlinear. Nevertheless, the constraints presented in Fig. 6 give us a rough idea of what to expect from the real data. We have also checked that increasing the fiducial converted fraction to $\zeta = 0.1$ only modestly strengthens constraints on κ.

We now proceed to describe our data and methodology.

III. METHODOLOGY

We follow the general scheme for the ΛCDM extension model analysis of the DES-Y1 3x2pt combined probes, which was described in detail in the DES-Y1 extensions paper [97]. In this section we will mainly focus on the methodology and systematics tests results specifically for the DMDR model, for full details, see Refs. [22,97].

A. Theory prediction pipeline

Our theory predictions for the DES 3x2pt data vector are derived from the 2D projection of the 3D matter and Weyl potential power spectra, incorporating complexities like nonlinear physics, galaxy bias, intrinsic alignments, photo-z bias, and shear calibration bias. The detailed derivation of 3x2pt theory prediction were described in Sec. IV.A of Ref. [22]. Here we only go through the procedures that are specifically modified for the DMDR model.

We first modify the Boltzmann code CAMB by implementing the equations described in Sec. II, and refer to this modified version as DMDR-CAMB. We also add a flag on σ_8 to ensure numerical stability in the nonlinear subroutine of DMDR-CAMB by attributing zero likelihood to models with $\sigma_8 > 1.4$ or $\sigma_8 < 0.4$. The resulting filter prior $\sigma_8 \in [0.4, 1.4]$, is about $\sim 10\sigma$ wide on each side of the fiducial value (relative to the DES-Y1 ΛCDM analysis [22], $\sigma_8 = 0.807^{+0.062}_{-0.041}$), and thus not expected to affect the overall constraints.

Next, the relation between the different cosmological quantities in the flat universe is enforced differently in DMDR comparing to ΛCDM because of a larger fraction of radiation density. The flat-universe relation is

$$\Omega_m + \Omega_\Lambda + \Omega_{\rm dr} = 1. \tag{17}$$

Specifically, while in ΛCDM the flatness condition implies $\Omega_\Lambda = 1 - \Omega_m$, in flat DMDR we enforce $\Omega_\Lambda = 1 - \Omega_m - \Omega_{\rm dr}$ instead.

Finally we improve upon the usual assumption that the Weyl potential Φ is completely contributed by matter in the late universe, $\Phi = \frac{3}{2}\Omega_m H_0^2 \delta_m / ac^2$. Recall the Weyl potential defined via the metric potentials ϕ and ψ in Newtonian gauge:

$$\begin{aligned} \Phi &= (\phi + \psi)/2, \\ ds^2 &= a^2(-(1+2\psi)dt^2 + (1-2\phi)dx^2). \end{aligned} \tag{18}$$

The assumption that the Φ power spectrum is proportional to the matter power spectrum is only reliable for negligible amounts of relativistic species in the late Universe, which holds in ΛCDM but can break in DMDR models with large ζ. At super-horizon scales, Φ diverges from the local matter perturbation. Our strategy is to take the appropriate ratio between the linear Weyl potential power spectrum $P_{\Phi\Phi}^{\rm lin}$ and the linear matter power spectrum $P_{\delta\delta}^{\rm lin}$, and then modify the shear clustering, galaxy clustering, and galaxy-galaxy power spectra. The Weyl-corrected (WC) power spectra are

$$P_{XX}^{\rm WC} = R_{\rm Weyl} P_{XX}, \tag{19}$$

$$P_{gX}^{\rm WC} = R_{\rm Weyl}^{1/2} P_{gX}, \tag{20}$$

with the dimensionless Weyl-correction factor defined as

$$R_{\rm Weyl} \equiv \frac{P_{\Phi\Phi}^{\rm lin}}{[\frac{3}{2}\Omega_m H_0^2 (z+1)^2/c^2]^2} \frac{1}{P_{\delta\delta}^{\rm lin}}, \tag{21}$$

where $X \in \{\gamma, \mathrm{IA}\}$ is a component of the correlation function that needs the Weyl correction (specifically, the shear and intrinsic alignments), and g stands for the galaxy position. Hence $P_{XX}^{\rm WC}$, $P_{gX}^{\rm WC}$ are building blocks for the corresponding projected (two-dimensional) angular correlation functions; for example $P_{\delta\delta}^{\rm WC}$ is used for the calculation of 2D lensing shear power. The physical reason that the IA and shear components require the gravitational potential correction is that these processes are directly determined by the gravitational field; galaxy shear is formed by the bending of light in the gravitational field, and IA is induced by the tidal gravitational field generated by nearby mass.

The Weyl potential and Newtonian potential in principle differ because they depend on different gravitational fields. In practice, we find that their relative difference is $< 1\%$ throughout the expansion history in a not-strongly-anisotropic metric in both DMDR and ΛCDM. We are thus justified in calculating the correction ratio in Eq. (21) from the Weyl-potential power spectrum. We further assume that Weyl-potential correction is linear and commutes with intrinsic alignments and galaxy bias (this dramatically simplifies the implementation in the code). While this is not guaranteed to be true, given the current linear modeling of intrinsic alignments and galaxy bias any leading-order adjustment is likely absorbed by the nuisance parameters. Any scale-dependent caveats of this assumption should be further suppressed by the fact that we adopt conservative scale cuts to limit the impact of uncertainties in the modeling of nonlinearities,

Lastly, as discussed in Sec. II D, we adopt Takahashi *et al.* halofit prescription [93] to produce the nonlinear matter power spectrum. We ensure the robustness of our analysis to small-scale physics by cutting out the data points at nonlinear scales as described in [97].

In Appendix A we include a comparison between Y1 analysis pipeline and our DMDR pipeline when both are applied to the ΛCDM mock data vector. It illustrates that the pipeline modifications do not induce noticeable bias ($\lesssim 0.1\sigma$).

TABLE II. Additional parameters used in the analysis with external datasets, along with their priors.

Parameter	Prior
Cosmological	
τ	Flat (0.01, 0.2)
Supernovae parameter	
M	Flat (−20.0, −18.0)
Planck-lite nuisance parameter	
$a_{\rm Planck}$	Gauss (1.0, 0.0025)

B. Parameters and priors

The DES 3x2pt data analysis applied to the DMDR model includes a total of 28 parameters; they are listed in Table I. There are eight cosmological parameters and 20 nuisance parameters. DMDR introduces two additional cosmological parameters to the usual six ($\Omega_m, h, \Omega_b, n_s, A_s, \Omega_\nu h^2$): the fraction of the converted dark matter ζ and the dark-matter conversion rate κ. When combining DES 3x2pt dataset with the external datasets, three more parameters, the reionization optical depth τ, supernova absolute magnitude M, and the Planck-lite likelihood nuisance parameter $a_{\rm Planck}$ are added into the variables. Their priors are presented in Table II.

The prior on ζ is flat in the range $\zeta \in [0.0, 1.0]$. This range is bounded by the limit when there is no dark-matter conversion, and the limit when half of the dark matter has converted since the primordial time. The latter choice is based on the fact that the early time Planck measurement of the matter density, $\Omega_m = 0.3166 \pm 0.0084$ [1], is within 20% of the late-time DES measurement, $\Omega_m = 0.264^{+0.032}_{-0.019}$. Hence, there is no indication that a large fraction of the dark matter has converted at $z \lesssim 1000$; this conclusion is also in line with previous work [40,41,46,101].

The prior on the conversion rate κ is also flat, with the range $\kappa \in [10^{-7}, 2]$. We set the lower bound very slightly above zero in order to ensure numerical stability of the modified code, and checked that in this small-κ limit the observables agree with those of ΛCDM. The upper prior limit is determined by the fact that neither the matter power spectrum nor the CMB angular power spectrum varies at a detectable level when $\kappa > 2$. This, in turn, can be understood from the evolution of the dark matter density illustrated in Fig. 1. When the conversion rate is as high as 2, new physics happened well after recombination and in the late stages of structure formation, allowing the DMDR model to mimic a ΛCDM universe with a higher density of dark matter. Thus models with $\kappa \gtrsim 2$ display a strong degeneracy between the new parameters (ζ, κ) and Ω_m, and are difficult to constrain tightly. It is important to keep this in mind when interpreting the κ posterior when it is pushed to the upper prior bound.

The cosmological parameters have flat priors that are nearly the same as in DES-Y1 (there are a few very minor differences between the two), and the nuisance parameters that model tomographic intrinsic alignments effect, photo-z uncertainty, shear calibration, and galaxy bias have the same Gaussian priors as in the DES-Y1 3×2 analysis [22]. We also impose a hard filter on the derived parameter σ_8 within [0.4, 1.4] as described in Sec. III A.

C. Datasets

Our cosmological parameters analysis will be performed on DES-Y1 3x2pt datasets, external datasets, and the combination of all datasets separately.

We first describe the DES-Y1 "3x2pt" measurements; here 3x2pt refers to three sets of two-point correlation functions as follows. Let i and j denote source-redshift bins (out of four total), and a and b denote the lens bins (out of five total). The correlation functions that form a set of observables that we call the "data vector" are as follows:

(i) $\xi_{\pm}^{ij}(\theta)$, the correlation between galaxy shear measured in source bins i and j.
(ii) $\gamma_t^{ib}(\theta)$, the cross-correlation between the galaxy shear in source bin i and the galaxy positions in lens bin a.
(iii) $w^{ab}(\theta)$ the correlation between galaxy positions in lens bins a and b.

The five redshift bins of the lens galaxy catalog are processed using redMaGiC [102]

$$z = [(0.15\sim 0.3),(0.3\sim 0.45),(0.45\sim 0.6),(0.6\sim 0.75),(0.75\sim 0.9)],$$

while the four redshift bins of the source galaxy catalog, obtained using the process called METACALIBRATION [103], are

$$z = [(0.2\sim 0.43),(0.43\sim 0.63),(0.63\sim 0.9),(0.9\sim 1.3)].$$

Each tomographic two-point correlation function has 20 log-spaced angular bins in the range $2.5' < \theta < 250'$, and a total of 45 tomographic angular correlation functions in each theta bin, for a total of $20\times 45 = 900$ data points. Cutting out small angular scales to avoid uncertainties with modeling nonlinearities (see Sec. II D) leaves 334 measurements. We refer the reader for other details, including those of theoretical modeling, to [22]. Treatment of some details specific for the DMDR is discussed in Sec. III A.

Now we describe the external datasets that we adopt; they are

(i) CMB: *Planck*-2018 high-ℓTT, TE, EE, polarization modes temperature spectra with $\ell \geq 30$ from Plik-lite likelihood, and TT, EE of the low-ℓ, $\ell \leq 29$ from Commander and SimAll likelihood, plus lensing potential C_ℓs with multipoles $8 \leq L \leq 400$ from SMICA likelihood [1,104].
(ii) Type Ia supernovae: we adopt the binned Pantheon SNe Ia dataset [77] covering the redshift range $0.01 < z < 2.3$.
(iii) BAO: we adopt the BOSS DR12 [78] measurements of $Hr_s/r_s^{\rm fid}$, $D_m r_s^{\rm fid}/r_s$ at redshifts [0.38, 0.51, 0.61], the SDSS-MGS [79] measurement of $\alpha = (D_V/D_V^{\rm fid})(r_s^{\rm fid}/r_s)$ at redshift 0.15, and the 6dFGS [80] measurement of r_s/D_V at redshift 0.106. The BOSS DR12 data come with a full covariance matrix, while all other data points only have diagonal uncertainties.

We do not include the redshift space distortion (RSD) measurements that we previously used in the DES + External data analysis [97]. We make this choice because DMDR allows for a scale-dependent growth of linear density perturbations, and the bias on $f\sigma_8$ measurements could be significant when the default ΛCDM templates are used in the compression of RSD information in the presence of a scale-dependent growth [105,106].

D. Samplers

For our principal results—constraints in the multidimensional parameter space—we use POLYCHORD [107]. POLYCHORD is a nested sampler with outstanding performance on Bayesian evidence estimation, which is useful for tension and model comparison analysis. We set POLYCHORD live_points = 250, num_repeats = 60, and tolerance = 0.1. This combination of settings was optimized to obtain precise and accurate results—especially in regards to the Bayesian-evidence computation—given our available CPU time.

We also need to run a number of chains for our systematic tests (shown further below in Fig. 7). High-quality nested-sampler runs are too time-consuming to be used for these runs. We thus make use of a couple of alternative numerical tools. First, we use the MULTINEST [108] sampler, which is faster than POLYCHORD. We use the MULTINEST sampler with settings live points = 250, efficiency = 0.3, and tolerance = 0.01. Second, we adopt our own importance sampler.

We use these two in conjunction as follows. We first run a baseline chain on uncontaminated theory predicted data vector, and save 334 3x2pt data points for each sample in the chain file. For the importance sampling, we reweight the samples by a factor $w_{\rm new} = [\mathcal{L}_{\rm new}/\mathcal{L}_{\rm old}]w_{\rm old}$, where $\mathcal{L}_{\rm old}$ is the old likelihood from the Monte-Carlo Markov chain (MCMC), and $\mathcal{L}_{\rm new}$ is the new likelihood calculated using the systematics contaminated data vector and the theory 3x2pt saved for the MCMC samples. In this way, the importance sampler can produce a chain for certain systematic tests in minutes, as opposed to days which running the theoretical pipeline at each sample would take. This process is therefore very CPU time efficient, but it is only valid in cases when importance sampling is representative on the baseline samples, and when the parameter space remains the same. Because sample systematics

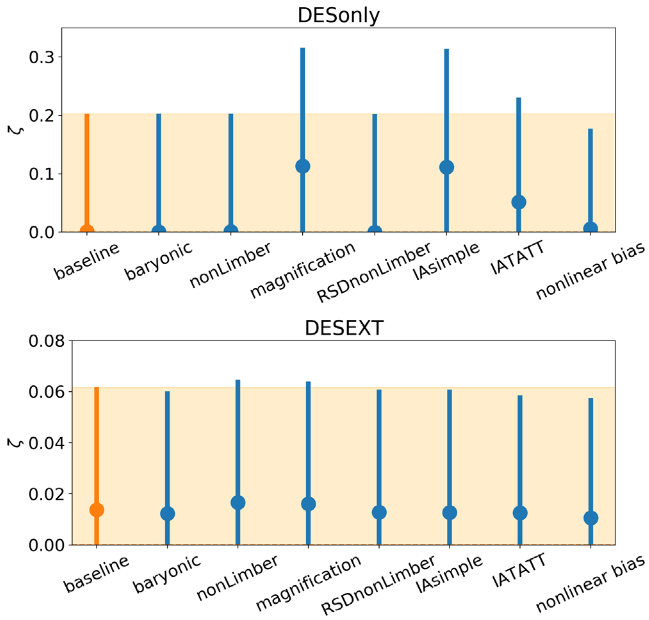

FIG. 7. The effect of different systematics biases on ζ for DES-only (top) and DES + EXT (bottom) analysis. The only systematics that show a visible impact are the magnification and intrinsic alignments for the DES-only data, causing a $\approx 0.5\sigma$ bias on ζ. All other systematics studied here lead to negligible biases.

considered in our tests happen to lead to small deviations from the fiducial model—thanks to our adoption of linear-only scales and nuisance parameters to model general systematics—this assumption is justified. Quantitatively, the criterion for the effectiveness of the importance sampling is given by the effective sample size (ESS) given by $\mathrm{ESS} = (\sum w)^2 / \sum (w^2)$. We regard importance sampling as trustworthy if post-importance sampling ESS preserves $\gtrapprox 0.8$ of the baseline ESS, and this is satisfied for all of our systematic tests that use importance sampling.

In summary, for the real data chains we used POLYCHORD as the sampler. The systematic tests using the importance sampler are the baryonic, non-Limber, magnification, and RSD non-Limber effects. The IA systematics are modeled by nuisance parameters, so they cannot use importance sampling. We run MULTINEST chain for the two IA systematics validation.

Now we proceed to the validation of pipeline robustness against systematics.

E. Systematics tests

Systematic errors, both theoretical and observational, are always a worry for large-scale structure analyses. To address this, we adopt a two-pronged strategy. First, we restrict ourselves to linear scales only, as described in Sec. II D. Second, we perform a battery of validation tests by adding various systematic effects to the data and monitoring how the results on the key cosmological parameters change. We now describe this latter strategy.

We start from a noiseless ΛCDM mock data vector for DES and Planck; that is, corresponding power spectra that contain no stochastic noise and are centered on the concordance theory model. The Planck mock likelihood is based on the compressed likelihood work [99], centered at ΛCDM fiducial cosmology. The DES likelihood is identical to the one adopted in this analysis, using theory predicted mock data files. We calculate the cosmological constraints from this baseline case. We then add the systematic effects described in Sec. IV. A of DES-Y1 extended-models paper [97], corresponding to baryonic effects, Limber approximation, magnification bias, Limber approximation with redshift space distortion, two intrinsic alignment models, and nonlinear galaxy bias, to generate systematics contaminated data vectors. In each of those cases, we redo the cosmological analysis and evaluate the errors on the key parameters.

The results are shown in Fig. 7 for the DES-only case (upper panel) and DES + EXTERNAL dataset (lower panel). We see that the systematics are causing at most 0.5σ bias in dark-matter converted fraction ζ in DES-only analysis, and no noticeable bias is observed when for the combination of DES and External datasets. The slight deviation ($\sim 0.2\sigma$) between the best-fit value of ζ and the assumed ΛCDM input $\zeta = 0.0$ is most likely due to the fact that we ran this test with synthetic DES likelihood but real BAO and supernovae data, and the latter two are not enforced to recover the input-model parameter values.

Because the fiducial simulated data vector is at the ΛCDM cosmology, κ is not constrained and no interesting conclusion could be made on systematic bias. We therefore conclude that our results are robust to some of the key systematic errors, at least to the extent that our systematic models represent the real-world errors.

F. Blinding

We blinded our real data analysis in the following way. After obtaining the MCMC chain on the real data, before unblinding the cosmological results, we added a random number scaled by the variance of the parameter to the MCMC samples. During the blinded stage of the analysis, we carried out the postprocesses including 2D contour plots and marginalized parameter constraints on these shifted samples. Our blinding preserves the shape of the contours with random shifting. Thus before proceeding to unblinding, we checked that the contour shapes are reasonable for the data constraining power, and the last few samples have the likelihoods at correct order of magnitude (they are usually not the max a posteriori). In the end we unblinded the cosmological results by resuming the raw samples of the real data MCMC chain. No change to the pipeline was done after unblinding, for the results reported in the next section. The real data analysis pipeline is completely consistent with the systematics test in the above subsection.

IV. RESULTS

We now present our constraints on DMDR cosmology, followed by the tension and model-comparison results.

A. Constraints on DMDR model

The constraints on DMDR parameters ζ and κ are shown in Fig. 8, and their 1D marginalized statistics summarized in Table III. For the converted dark-matter fraction ζ, we find

$$\zeta < 0.32 \quad \text{DES-only}, \tag{22}$$

$$<0.030 \quad \text{External-only}, \tag{23}$$

$$<0.037 \quad \text{DES + External}. \tag{24}$$

Note that we see a slightly looser constraint on ζ with DES + External dataset than External-only dataset. This is somewhat counterintuitive, as our forecast predicted that weak lensing and galaxy clustering would tighten the constraint on ζ by anchoring the matter density at low redshift. However the Fisher forecast of course assumes Gaussian likelihood in all parameters. In the presence of

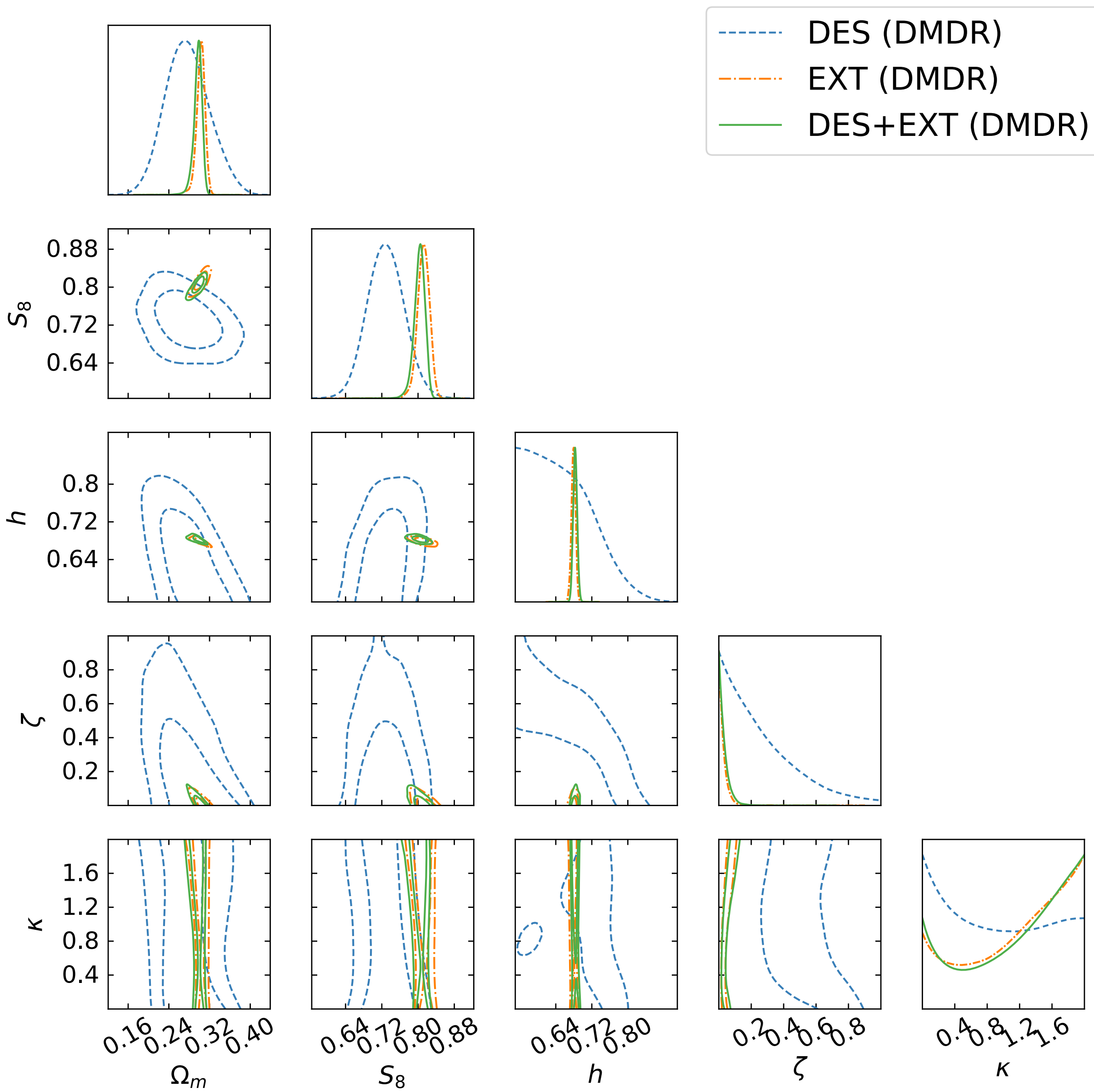

FIG. 8. Constraints by DES-only, External-only, and DES + External data on the converted dark-matter fraction ζ and rate κ, along with those on Ω_m, S_8, and h.

TABLE III. 1D marginalized statistics of cosmological parameters. The means of the marginalized 1D posteriors and 1σ confidence levels are reported, with global maximum posterior sample in the parenthesis. The dashed lines mean that there is no constraint on the parameter (but we report the global posterior maximum), while the N/A means that the parameter is not relevant to the model studied. For the DES-only DMDR constraint, the global best fit of Ω_m is about 2σ away from the mean value, possibly due to the $\zeta - \Omega_m$ degeneracy. The degeneracy is broken for the External and DES + External datasets, when information from a wide redshift range is taken into consideration.

	h	Ω_m	S_8	ζ	κ
DES (DMDR)	$<0.68(0.64)$	$0.276^{+0.039}_{-0.046}(0.346)$	$0.729 \pm 0.040(0.700)$	$<0.32(0.01)$	–(1.38)
DES (ΛCDM)	$<0.69(0.72)$	$0.310^{+0.035}_{-0.040}(0.306)$	$0.726 \pm 0.039(0.723)$	N/A	N/A
EXT (DMDR)	$0.6794 \pm 0.0046(0.6767)$	$0.3025^{+0.0091}_{-0.0069}(0.3113)$	$0.812 \pm 0.013(0.829)$	$<0.030(0.028)$	–(0.0033)
EXT (ΛCDM)	$0.6786 \pm 0.0046(0.6783)$	$0.3085 \pm 0.0059(0.3093)$	$0.819 \pm 0.011(0.826)$	N/A	N/A
DES + EXT (DMDR)	$0.6830 \pm 0.0045(0.6822)$	$0.2970^{+0.0091}_{-0.0062}(0.2994)$	$0.803^{+0.013}_{-0.010}(0.808)$	$<0.037(0.020)$	–(1.90)
DES + EXT (ΛCDM)	$0.6822 \pm 0.0043(0.6825)$	$0.3038 \pm 0.0054(0.3036)$	$0.809^{+0.010}_{-0.009}(0.808)$	N/A	N/A
SH0ES	0.740 ± 0.014	N/A	N/A	N/A	N/A

non-Gaussianities, especially in a high-dimensional space, combined constraints are often (slightly) worse than those from individual probes.

No constraint on conversion rate κ is obtained; see the bottom right of Fig. 8. This agrees with the expectation that κ is unconstrained in the limit when the amount of converted dark matter, ζ, is very small.

We can see a raising posterior profile towards the upper bound of the κ prior. Although not statistically meaningful, such posterior profile suggest that we possibly underestimated the prior upper bound. Other explanations include the IA systematics and high-dimensional parameter space geometry. In any case, higher κ, namely even faster conversion that happens at extremely low z is still open for investigation. However exploration of this avenue requires a more specific analysis, similar to one in models with a late dark-energy transition [109] in order to take the distance-ladder calibration into consideration. Hence we leave this for future work.

Other cosmological parameters that are of interest because they are tightly constrained or exhibit tensions between surveys—h, Ω_m and $S_8 = \sigma_8\sqrt{\Omega_m/0.3}$—are also illustrated in the triangle plot Fig. 8, and summarized in Table III.

B. Model comparison and tensions

As the tension between early and late Universe surveys draws more and more attention in the cosmology community, there has been increasing number of works dedicated to quantify the concordance and discordance into statistical metrics [110–112]. In this work, we quote Bayesian evidence and maximum *a posteriori* (MAP) χ^2 difference as the model-comparison metrics, and use the "suspiciousness" metric defined in reference [111]. We also report the one-dimensional differences in units of error bars for the parameters suspected to be tension, i.e., h, Ω_m, and S_8. We stress that we avoid combining any datasets that are known to be in tension, such as *Planck* and distance ladder (for h) or *Planck* and DES (for S_8).

We now report the model-comparison results.

(i) χ^2 at MAP Cosmology. A very traditional criterion of the goodness of a model is the χ^2 evaluated at the maximum *a posteriori* parameter values $\chi^2_{\mathrm{MAP}} = (d-M)^{\mathrm{T}}C^{-1}(d-M)|_{\mathrm{MAP}}$, where d is the full dataset, M is the theory prediction evaluated at the maximum posterior sample, and C is the covariance matrix of the full dataset. A preferred model should have smaller MAP χ^2, and be punished by the number of extra parameters. Due to the non-Gaussianity and the different normalization scheme of different survey likelihoods, we choose to report the effective χ^2 defined as

$$\chi^2_{\mathrm{MAP}} = -2\log\mathcal{L}|_{\mathrm{MAP}}. \tag{25}$$

We ran an optimizer three times, adopting the scipy optimizer with Nelder-Mead method to calculate the MAP from the POLYCHORD chain samples; from these we report the best final MAP value. The χ^2 difference between the DMDR and ΛCDM model is

$$\begin{aligned} \Delta\chi^2_{\mathrm{MAP}} &= -0.6 \qquad \text{DES-only}, \\ &= +0.8 \qquad \text{External-only}, \\ &= +0.1 \qquad \text{DES + External}, \end{aligned} \tag{26}$$

as summarized in Table IV. Therefore our DMDR model does not give a substantially better global fit to the data than ΛCDM.

(ii) Bayesian evidence ratio. Bayesian evidence $\mathcal{Z}$ is defined as

TABLE IV. Difference in $\chi^2_{\rm MAP}$, evaluated at the maximum *a posteriori* point in parameter space, between DMDR and ΛCDM for different dataset combinations.

	DES-Y1 3x2pt	Planck2018-CMB	Planck2018-lensing	Pantheon	6dFGS	BOSS DR12	MGS	Total
DES $\Delta\chi^2_{\rm MAP}$	−0.6							−0.6
EXT $\Delta\chi^2_{\rm MAP}$		0.0	0.0	0.1	0.1	0.7	−0.1	0.8
DES+EXT $\Delta\chi^2_{\rm MAP}$	0.7	−0.4	−0.4	−0.0	0.0	0.3	−0.1	0.1

$$\mathcal{Z} = \int \mathcal{L}(d|\theta)\Pi(\theta)d\theta, \tag{27}$$

where $\mathcal{L}$ is the likelihood, d is the data vector, and θ are the model parameters. We report $\mathcal{Z}$ reported by the nested sampler POLYCHORD, with statistics done by ANESTHETIC [113].[5] The evidence ratio could be interpreted as the probability of two models given data through [114]:

$$\frac{P(\mathrm{DMDR}|d,I)}{P(\Lambda\mathrm{CDM}|d,I)} = \frac{P(\mathrm{DMDR}|I)}{P(\Lambda\mathrm{CDM}|I)}\frac{\mathcal{Z}(\mathrm{DMDR})}{\mathcal{Z}(\Lambda\mathrm{CDM})}, \tag{28}$$

where I is the prior that these two models are in the consideration. Assuming no prior preference for either DMDR or ΛCDM, namely $P(\mathrm{DMDR}|I) = P(\Lambda\mathrm{CDM}|I)$, the ratio of DMDR and ΛCDM probabilities is equal to the ratio of their respective evidences $\mathcal{Z}$. These, in turn, are reported by the POLYCHORD sampler; their ratio is

$$\begin{aligned} K = \frac{\mathcal{Z}(\mathrm{DMDR})}{\mathcal{Z}(\Lambda\mathrm{CDM})} &= 0.31 \qquad \text{DES-only},\\ &= 0.03 \qquad \text{External-only},\\ &= 0.09 \qquad \text{DES + External}. \end{aligned} \tag{29}$$

We interpret the Bayesian evidence ratio in terms of the Jeffreys' scale (making this also consistent with DES-Y1 paper [22]). Assuming an equal prior on ΛCDM and DMDR model, $0.31 < K < 1.0$ would indicate no conclusive preference for either model, $0.1 < K < 0.31$ would imply substantial evidence favoring ΛCDM, $0.031 < K < 0.1$ would imply strong evidence favoring ΛCDM, and $K < 0.031$ would imply very strong evidence favouring ΛCDM [115,116].

Under Jeffreys' scale, our results therefore indicate that the DES-Y1-only dataset does not prefer either DMDR or ΛCDM, while the External-only dataset very strongly disfavors the DMDR model. Finally the combination of all datasets strongly disfavors DMDR.

[5] https://github.com/williamjameshandley/anesthetic.

(iii) Suspiciousness. This tension statistic [111] has the merit of being less affected by the choice of the priors than Bayesian evidence. Suspiciousness $\mathcal{S}$ is defined in terms of the Bayesian evidence ratio R and information ratio I:

$$\log\mathcal{S} = \log R - \log I, \tag{30}$$

where

$$R = \frac{\mathcal{Z}_{AB}}{\mathcal{Z}_A\mathcal{Z}_B} \tag{31}$$

$$\log I = \mathcal{D}_A + \mathcal{D}_B - \mathcal{D}_{AB} \tag{32}$$

$$\mathcal{D} = \int \mathcal{P}(\theta)\log\frac{\mathcal{P}(\theta)}{\Pi(\theta)}d\theta, \tag{33}$$

where $\mathcal{D}$ is the Kullback-Leibler divergence of the posterior against prior, quantifying the information gained by the data. The calculation of suspiciousness requires our knowledge of the posterior $\mathcal{P}$, prior Π, and evidence $\mathcal{Z}$ from MCMC chains. Here A and B stand for the DES-Y1 and External datasets that we are comparing, and AB for their combination. We report the $\log\mathcal{S}$ calculated by ANESTHETIC [113]:

$$\begin{aligned} \log\mathcal{S} &= -2.21, \qquad p = 0.08 \qquad \text{DMDR},\\ \log\mathcal{S} &= -2.93, \qquad p = 0.04 \qquad \Lambda\text{CDM}, \end{aligned} \tag{34}$$

where each p value is interpreted as the probability that datasets A and B can be both described by the parameters of the model. We therefore find that DMDR reduces the tension between DES and the external data, as indicated by a higher p value, at the expense of two new parameters.

(iv) Hubble and S_8 tensions. We now specifically investigate the impact of the new freedom in DMDR to two widely discussed tensions in ΛCDM: the $4-5\sigma$ tension in the (scaled) Hubble constant h between CMB and local measurements, and the $2-3\sigma$ tension in S_8 between CMB and weak lensing plus clustering. We take the probability distribution of the parameter difference $\Delta h = h_A - h_B$ or, alternatively, $\Delta S_8 = S_{8,A} - S_{8,B}$, from the 1D marginalized probability distribution obtained by different datasets.

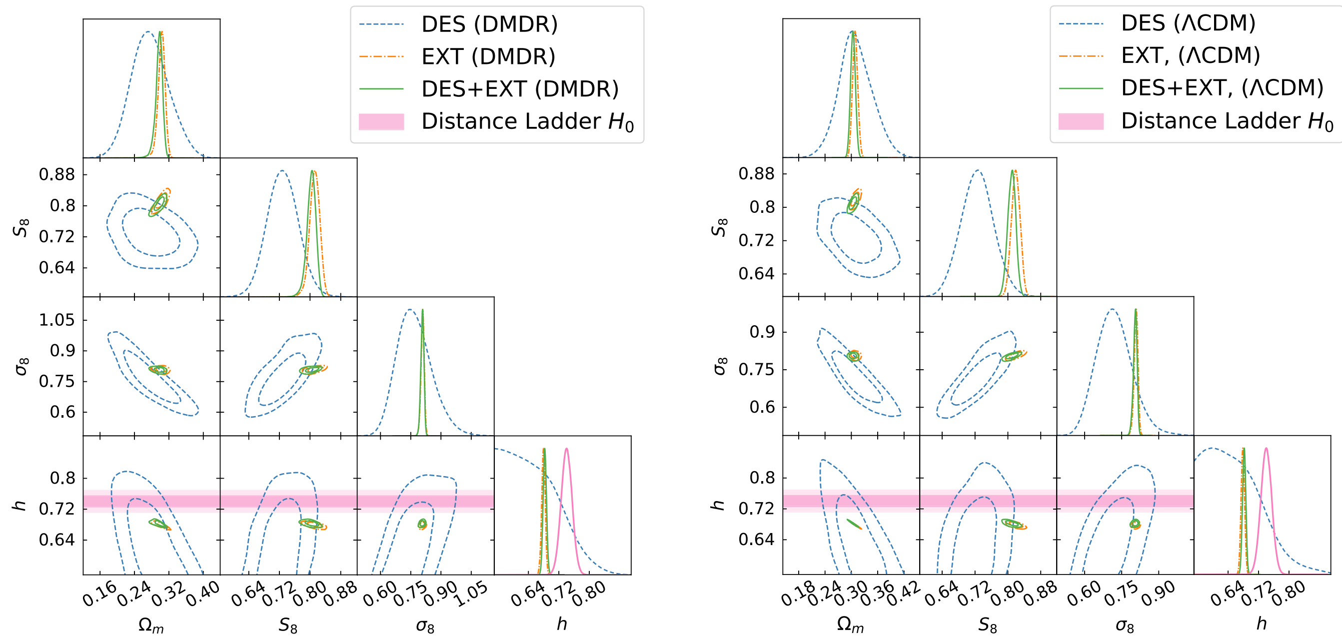

FIG. 9. Left panel: cosmological parameters Ω_m, S_8, σ_8, h constraints in DMDR model, reported for DES, External, and DES + External datasets, together with the local Hubble measurement [117] in pink. Right panel: same plot in the ΛCDM cosmology. By comparing the panels involving σ_8, S_8 on both sides, we can see how DMDR reduced the tension in the matter density fields between DES and the CMB + Supernovae + BAOs.

Here A and B are the two datasets between which we want to estimate the tension (in either h or S_8). For a cosmological parameter of interest θ, we integrate over the interval bounded by the $\Delta\theta$ values that have the equal posterior, and one of the boundaries is $\Delta\theta = 0$. Thus we get the tension probability p:

$$p = \int_{\Delta\theta=0}^{\text{eq-post}} P(\Delta\theta = \theta_A - \theta_B) d\Delta\theta. \quad (35)$$

We then interpret p into $z - \sigma$ tension using

$$p = \text{erf}\left(\frac{z}{\sqrt{2}}\right). \quad (36)$$

For the tension in the Hubble parameter, the dataset A is the full DES + CMB + Supernovae + BAO data, while dataset B is the Gaussian-distributed constraint on h from the distance-ladder measurement [117]. For the ΔS_8 tension, our A dataset is the DES-Y1 3x2pt-only data, while B is the CMB + Supernovae + BAO External dataset. The enlarged constraints on Ω_m, S_8, σ_8, and h are illustrated in Fig. 9, overplotted with the distance ladder measurement of H_0 from [117]. We find that

(a) When comparing the DES + External datasets with local Hubble measurement in [117], $h = 0.7403 \pm 0.0142$, the tension in h assuming either DMDR or ΛCDM is 3.8σ.

(b) When comparing DES-Y1 dataset with External dataset, the tension in S_8 is 1.9σ for DMDR model, slightly reduced from 2.3σ for ΛCDM model.

Hence our DMDR model does not substantially alleviate the Hubble tension, but does help in reducing the S_8 tension.

V. CONCLUSIONS

In this work, we test a late-time dark-matter to dark-radiation conversion model, dubbed the DMDR model, against cosmological data. Our model is specified by two new parameters defined in Eqs. (1) and (2): the fraction of dark matter that has converted ζ, and the rate of its conversion (to dark radiation) κ. We work out the perturbation equations in this model, and incorporate them in the Einstein-Boltzmann code CAMB [82]. Our analysis pipeline is modified for the DMDR model in the following respects. (1) We scale-dependently correct the shear and intrinsic alignment terms in the two-point correlation functions to account for the non-trivial relation between gravitational field and matter density perturbation field, and (2) we adopt conservative scale cuts to protect the analysis against systematic errors due to the modeling of clustering on nonlinear scales. In our analysis, we principally consider the DES-Y1 "3x2pt" (weak lensing and galaxy clustering) data. We also study the impact of adding external datasets: Planck-2018 CMB power spectra (TT, TE, EE, and lensing spectrum); Pantheon compilation of type Ia supernovae data; and compressed BAO measurements from BOSS-DR12, MGS, and 6dFGS surveys.

The constraint on the fraction of the converted dark matter obtained from all data combined is $\zeta < 0.037$. We find no constraint on the conversion rate parameter κ as expected in the limit when $\zeta \to 0$. We further find that the evidence-ratio test applied with the full combined data does not favor the DMDR model compared to ΛCDM. DMDR does however reduce the suspiciousness tension metric between DES-Y1 and the combination of CMB, Supernovae, and BAO data, raising the probability that DES and external data are concordant from 4% to 8%. Finally, DMDR does not help in alleviating the Hubble tension but does reduce the tension in the DES and external-data measurements of $S_8 = \sigma_8\sqrt{\Omega_m/0.3}$, making it go from 2.3σ (in ΛCDM) to 1.9σ (in DMDR).

We stress that the above conclusions are drawn for the late Universe dark-matter-dark-radiation conversion model introduced in Sec. II A. Further generalizations of this catalog [31,32,34–48], for example where dark matter is a composition of some fraction of interacting dark matter and cold dark matter, or where the transition time is short, or the transition occurs in the early Universe, were not considered in this work. These variants could in principle better fit the background evolution of the Universe than the model we studied, and are thus a promising target for further investigations.

There are several other directions in which our analysis could be extended. One possibility is to model the non-linear matter power spectrum in real and redshift space in DMDR models [96,118,119]. This could be particularly helpful for DES year-3 and year-6 data which have more statistical power and where pushing to smaller, nonlinear scales could improve the constraints. Another future direction is to enable the use of the uncompressed BAO data (that is, the broadband galaxy and quasar power spectra). This would potentially improve the constraints for not only the DMDR model but also other beyond-ΛCDM models, and could become an important analysis tool for future surveys such as those to be undertaken by DESI, the Rubin Observatory (LSST), Euclid, and the Roman Space Telescope.

Our investigation was limited to galaxy clustering, weak lensing, and galaxy-galaxy lensing which are united in the so-called 3×2 analysis. Recent years have seen the emergence of new, promising cosmological probes which, when incorporated, could improve the constraints presented here. For example, the Lyman-α BAO measurements from high-redshift quasars and clustering obtained from the 21-cm signal could both be very helpful for constraining DMDR-type models where slow transition happen between $z\sim 1$ and recombination. The medium redshift measurements can fill in the blank in the current cosmological observations concentrated on two ends of the time stretch. It will be exciting to see if incorporating new cosmological probes and combining them with the improved 3×2 analyses from Stage IV dark-energy surveys can help shed light on DMDR-type models.

ACKNOWLEDGMENTS

We thank Professor Shanjie Zhang, Professor Jianming Jin, and Dr. Robert C. Forrey for the development of the Hypergeometric Function calculation routine used in our DMDR-CAMB. Funding for the DES Projects has been provided by the U.S. Department of Energy, the U.S. National Science Foundation, the Ministry of Science and Education of Spain, the Science and Technology Facilities Council of the United Kingdom, the Higher Education Funding Council for England, the National Center for Supercomputing Applications at the University of Illinois at Urbana-Champaign, the Kavli Institute of Cosmological Physics at the University of Chicago, the Center for Cosmology and Astro-Particle Physics at the Ohio State University, the Mitchell Institute for Fundamental Physics and Astronomy at Texas A&M University, Financiadora de Estudos e Projetos, Fundação Carlos Chagas Filho de Amparo à Pesquisa do Estado do Rio de Janeiro, Conselho Nacional de Desenvolvimento Científico e Tecnológico and the Ministério da Ciência, Tecnologia e Inovação, the Deutsche Forschungsgemeinschaft and the Collaborating Institutions in the Dark Energy Survey. The Collaborating Institutions are Argonne National Laboratory, the University of California at Santa Cruz, the University of Cambridge, Centro de Investigaciones Energéticas, Medioambientales y Tecnológicas-Madrid, the University of Chicago, University College London, the DES-Brazil Consortium, the University of Edinburgh, the Eidgenössische Technische Hochschule (ETH) Zürich, Fermi National Accelerator Laboratory, the University of Illinois at Urbana-Champaign, the Institut de Ciències de l'Espai (IEEC/CSIC), the Institut de Física d'Altes Energies, Lawrence Berkeley National Laboratory, the Ludwig-Maximilians Universität München and the associated Excellence Cluster Universe, the University of Michigan, NFS's NOIRLab, the University of Nottingham, The Ohio State University, the University of Pennsylvania, the University of Portsmouth, SLAC National Accelerator Laboratory, Stanford University, the University of Sussex, Texas A&M University, and the OzDES Membership Consortium. Based in part on observations at Cerro Tololo Inter-American Observatory at NSF's NOIRLab (NOIRLab Prop. ID 2012B-0001; PI: J. Frieman), which is managed by the Association of Universities for Research in Astronomy (AURA) under a cooperative agreement with the National Science Foundation. The DES data management system is supported by the National Science Foundation under Grants No. AST-1138766 and No. AST-1536171. The DES participants from Spanish institutions are partially supported by MICINN under Grants No. ESP2017-89838, No. PGC2018-094773, No. PGC2018-102021, No. SEV-2016-0588, No. SEV-2016-0597, and No. MDM-2015-0509, some of which include ERDF funds from the European Union. I. F. A. E. is partially funded by the CERCA program of the Generalitat de Catalunya. Research leading to these results has received funding from the European Research Council under the European Union's Seventh Framework Program (Grant No. FP7/2007-2013) including ERC Grants Agreement No. 240672, No. 291329, and No. 306478. We acknowledge support from the Brazilian Instituto Nacional de Ciência e Tecnologia (INCT) do e-Universo (CNPq Grant No. 465376/2014-2). This manuscript has been authored by Fermi Research Alliance, LLC under Contract No. DE-AC02-07CH11359 with the U.S. Department of Energy, Office of Science, Office of High Energy Physics.

APPENDIX A: PIPELINE COMPARISON ON ΛCDM

We want to make sure that, any cosmological parameters constraints that are found different from the DES-Y1 3x2pt Key paper [22] ones are physical, namely caused by the DMDR model, but not due to the pipeline choices variance. Hence we run full MULTINEST MCMC chains on the same ΛCDM simulated data vector, using DES-Y1 analysis

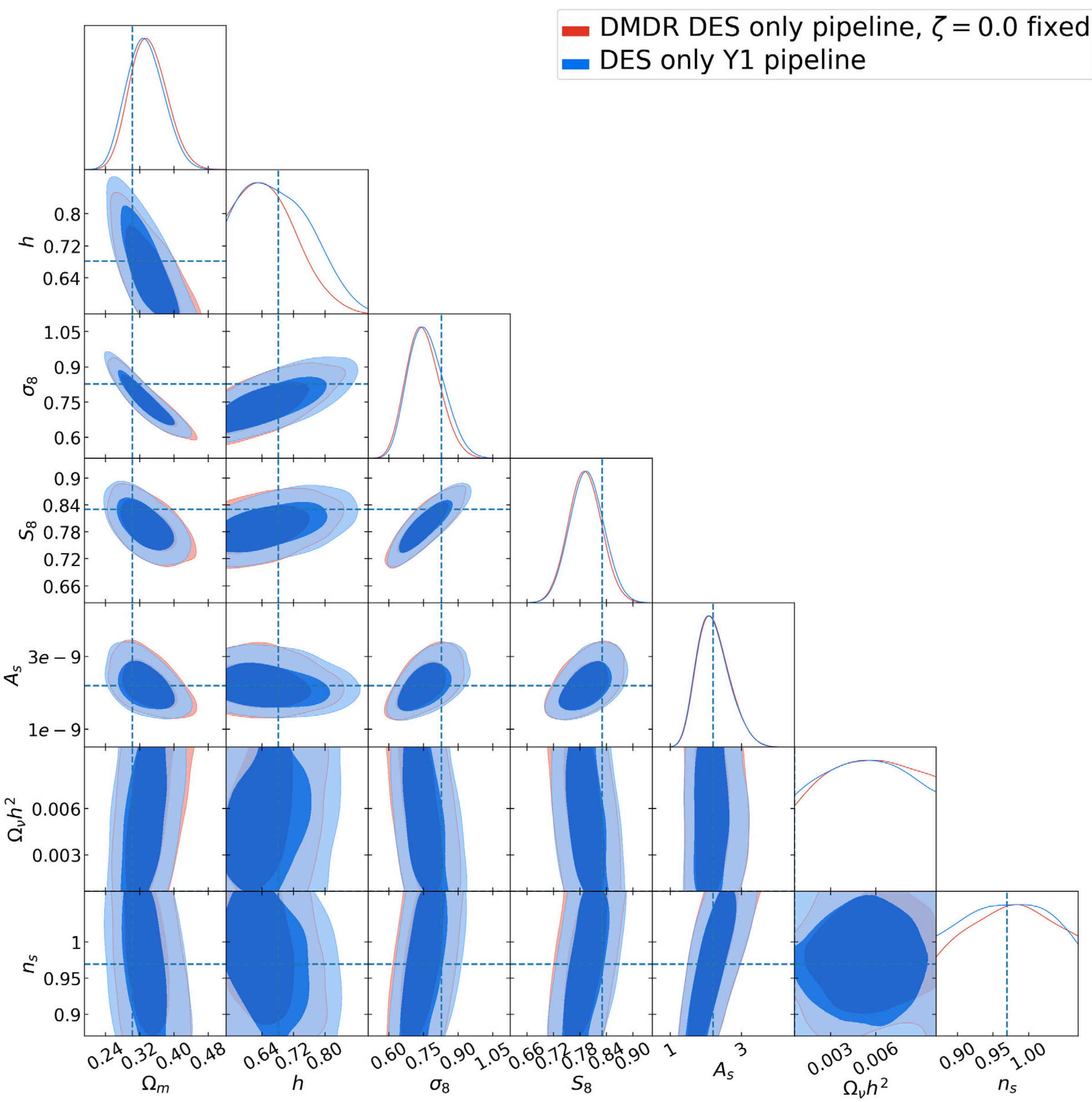

FIG. 10. Comparison of the constraints using DES-Y1 analysis pipeline (blue) and our DMDR analysis pipeline with new parameters fixed ($\zeta = 0.0$, $\kappa = 1.0$; red contours). We use a simulated ΛCDM data vector on which we apply the MULTINEST MCMC chains for both runs.

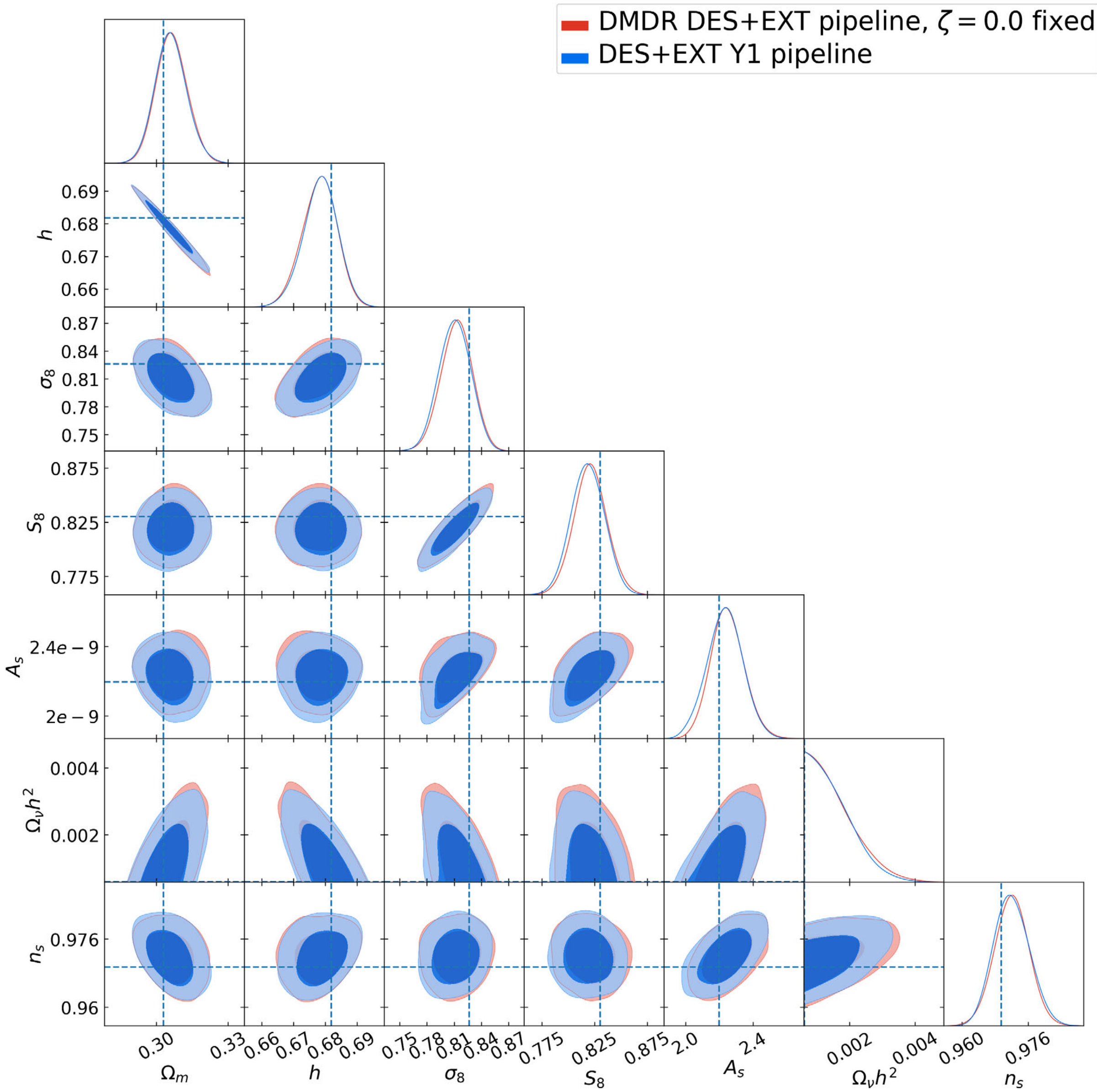

FIG. 11. Same as Fig. 10, but for DES-Y1 + External simulated data.

pipeline and our DMDR analysis pipeline with $\zeta = 0.0$, $\kappa = 1.0$ fixed (ΛCDM subspace, so κ value is irrelevant). The results are shown in Figs. 10 and 11 for DES only and DES + External data. In both cases, except for the parameters that are not effectively constrained like h, $\Omega_\nu h^2$, and n_s for DES only data, the posteriors from two pipelines agree with each other at $\lesssim 0.1\sigma$ level.

APPENDIX B: DARK RADIATION HIERARCHY EQUATIONS

In B18, perturbation equations were derived from the perturbation expansion of the energy-momentum tensor for dark matter and dark radiation,

$$T^{\rm dm}_{\mu\nu} = \bar{\rho}_{\rm dm}(1+\delta_{\rm dm})u^{\rm dm}_\mu u^{\rm dm}_\nu, \tag{B1}$$

$$T^{\rm dr}_{\mu\nu} = \frac{4}{3}\bar{\rho}_{\rm dr}(1+\delta_{\rm dr})u^{\rm dr}_\mu u^{\rm dr}_\nu + \frac{\bar{\rho}_{\rm dr}(1+\delta_{\rm dr})}{3}g_{\mu\nu} + \Pi^{\rm dr}_{\mu\nu}, \tag{B2}$$

where in synchronous gauge $u^{\rm dm}_\mu = a(1,\vec{0})$, $u^{\rm dr}_\mu = a(1,\vec{v}^{\rm dr})$. For dark matter and dark radiation defined in this way, we can write the continuity equations and Einstein equations as

$$\nabla^\nu T^{\rm dm}_{\mu\nu} = -\nabla^\nu T^{\rm dr}_{\mu\nu} = -\mathcal{Q}u^{\rm dm}_\mu \tag{B3}$$

$$R_{\mu\nu} - \frac{1}{2}Rg_{\mu\nu} + \Lambda g_{\mu\nu} = \frac{8\pi G}{c^4}T_{\mu\nu}, \tag{B4}$$

where $u_\mu^{\rm dm}$ is the proper velocity of the dark matter. Note that the right-hand side of the continuity equation has a collision term instead of zero for CDM. In B18 the dark radiation is only expanded up to $\delta_{\rm dr}$, $\theta_{\rm dr} = \partial_i v^i_{\rm dr}$ and one anisotropy shear $\Pi^{\rm dr}_{ij} = (\partial_i\partial_j - \frac{1}{3}\delta_{ij}\nabla^2)\Pi^{\rm dr}$, which is sufficient when dark radiation self-interacts or continues to interact with dark matter after produced so the higher ℓ terms damp out.

In our work, we assume dark radiation to be a completely free-streaming relativistic species and write down the full phase space perturbation hierarchy equations for it, which differs from the massless neutrino ones by a collision term. The phase space dynamics of the dark radiation with collision terms are [83]

$$\frac{\partial F_{\rm dr}(\vec{k},\hat{n},\tau)}{\partial\tau} + ik\mu F_{\rm dr}(\vec{k},\hat{n},\tau) = -\frac{2}{3}\dot{h}(\vec{k},\tau) - \frac{4}{3}(\dot{h}(\vec{k},\tau) + 6\dot{\eta}(\vec{k},\tau))P_2(\hat{k}\cdot\hat{n}) + \left(\frac{\partial F_{\rm dr}(\vec{k},\hat{n},\tau)}{\partial\tau}\right)_C. \tag{B5}$$

The phenomenology of the microphysics of the dark-matter to dark-radiation conversion process is mostly demonstrated in the collision term

$$\left(\frac{\partial F_{\rm dr}(\vec{k},\hat{n},\tau)}{\partial\tau}\right)_C = \frac{a}{\rho_{\rm dr}(a)}(-\mathcal{Q}(a)F_{\rm dr}(\vec{k},\hat{n},\tau) + \delta\mathcal{Q}), \tag{B6}$$

especially its perturbation part $\delta\mathcal{Q}$ which depends on the details of the interacting physical quantities like particle momentum. However, from several case studies in B18 on Sommerfeld enhancement and single-body decay processes, it seems that the precision of the current generation of cosmological observations is not sufficient to discriminate between the specific forms of $\delta\mathcal{Q}$. Hence we assume the simplest form of the collision perturbation $\delta\mathcal{Q} = \mathcal{Q}\delta_{\rm dm}$, without dependence on polarization or momentum anisotropy:

$$\left(\frac{\partial F_{\rm dr}(\vec{k},\hat{n},\tau)}{\partial\tau}\right)_C = \frac{\mathcal{Q}(a)a}{\rho_{\rm dr}(a)}(-F_{\rm dr}(\vec{k},\hat{n},\tau) + \delta_{\rm dm}(\vec{k},\tau)). \tag{B7}$$

Expanding $F_{\rm dr}$ in Eq. (B7) into harmonics, we get

$$F_{\rm dr}(\vec{k},\hat{n},\tau) = \sum_{l=1}^{\infty}(-i)^l(2l+1)F_{\rm dr}l(\vec{k},\tau)P_l(\hat{k}\cdot\hat{n}). \tag{B8}$$

Noticing that only $F_{\rm dr}(\vec{k},\hat{n},\tau)$ itself needs expansion, while other terms in Eq. (B7) are constant to the orientation variable $\hat{k}\cdot\hat{n}$, we get the following hierarchy equation [83,84,86,87]:

$$(J_l^{\rm dr})' = \frac{k}{2l+1}[lJ^{\rm dr}_{l-1} - \beta_{l+1}(l+1)J^{\rm dr}_{l+1}] + \frac{8}{15}k\sigma\delta_{l2} - \frac{4}{3}k\mathcal{Z}\delta_{l0} - \frac{aQ}{\bar{\rho}_{\rm dr}}J^{\rm dr}_l, \tag{B9}$$

where $J_0^{\rm dr} \equiv \delta_{\rm dr}$, $J_1^{\rm dr} \equiv q_{\rm dr} = \frac{4}{3}\theta_{\rm dr}/k$, $J_2^{\rm dr} \equiv \pi_{\rm dr} = \Pi^{\rm dr}/\bar{\rho}_{\rm dr}$ in CAMB convention, δ_{l0}, δ_{l2} are Dirac delta functions. Equations $l = 0$, $l = 1$ agree with the Eqs. (14) and (15) in B18.

[1] N. Aghanim, Y. Akrami, M. Ashdown, J. Aumont, C. Baccigalupi, M. Ballardini, A. Banday, R. Barreiro, N. Bartolo, S. Basak *et al.*, Planck 2018 results. vi. Cosmological parameters, Astron. Astrophys. **641**, A6 (2020).

[2] L. Verde, T. Treu, and A. G. Riess, Tensions between the early and late universe, Nat. Astron. **3**, 891 (2019).

[3] A. G. Riess, The expansion of the universe is faster than expected, Nat. Rev. Phys. **2**, 10 (2020).

[4] C. D. Huang, A. G. Riess, S. L. Hoffmann, C. Klein, J. Bloom, W. Yuan, L. M. Macri, D. O. Jones, P. A. Whitelock, S. Casertano *et al.*, A near-infrared period–luminosity relation for miras in ngc 4258, an anchor for a new distance ladder, Astrophys. J. **857**, 67 (2018).

[5] A. G. Riess, S. Casertano, W. Yuan, L. M. Macri, and D. Scolnic, Large magellanic cloud cepheid standards provide a 1% foundation for the determination of the Hubble constant and stronger evidence for physics beyond λcdm, Astrophys. J. **876**, 85 (2019).

[6] W. L. Freedman, B. F. Madore, D. Hatt, T. J. Hoyt, I. S. Jang, R. L. Beaton, C. R. Burns, M. G. Lee, A. J. Monson, J. R. Neeley *et al.*, The Carnegie-Chicago Hubble program. viii. An independent determination of the Hubble constant based on the tip of the red giant branch, Astrophys. J. **882**, 34 (2019).

[7] K. C. Wong, S. H. Suyu, G. C.-F. Chen, C. E. Rusu, M. Millon, D. Sluse, V. Bonvin, C. D. Fassnacht, S. Taubenberger, M. W. Auger *et al.*, H0licow xiii. A 2.4% measurement of h_0 from lensed quasars: 5.3\σ tension between early and late-universe probes, Mon. Not. R. Astron. Soc. **498**, 1420 (2020).

[8] E. Di Valentinoa, A. Melchiorrib, O. Menac, and S. Vagnozzid, Interacting dark energy in the early 2020s: A promising solution to the h0 and cosmic shear tensions, Phys. Dark Universe **30**, 100666 (2020).

[9] V. Poulin, T. L. Smith, T. Karwal, and M. Kamionkowski, Early Dark Energy Can Resolve the Hubble Tension, Phys. Rev. Lett. **122**, 221301 (2019).

[10] M.-X. Lin, G. Benevento, W. Hu, and M. Raveri, Acoustic dark energy: Potential conversion of the Hubble tension, Phys. Rev. D **100**, 063542 (2019).
[11] N. Blinov, C. Keith, and D. Hooper, Warm decaying dark matter and the Hubble tension, J. Cosmol. Astropart. Phys. 06 (2020) 005.
[12] J. Sola, A. Gomez-Valent, J. d. C. Perez, and C. Moreno-Pulido, Brans-dicke cosmology with a λ-term: A possible solution to λcdm tensions, Classical Quantum Gravity **37**, 245003 (2020).
[13] K. Jedamzik and L. Pogosian, Relieving the Hubble Tension with Primordial Magnetic Fields, Phys. Rev. Lett. **125**, 181302 (2020).
[14] E. Elizalde, M. Khurshudyan, S. D. Odintsov, and R. Myrzakulov, An analysis of the $h\_\{0\}$ tension problem in a universe with a viscous dark fluid, Phys. Rev. D **102**, 123501 (2020).
[15] X. Li and A. Shafieloo, Generalised emergent dark energy model: Confronting *lambda* and pede, Astrophys. J. **902**, 58 (2020).
[16] W. Yang, E. Di Valentino, S. Pan, and O. Mena, A complete model of phenomenologically emergent dark energy, Phys. Dark Universe **31**, 100762 (2021).
[17] L. Hart and J. Chluba, Updated fundamental constant constraints from planck 2018 data and possible relations to the Hubble tension, Mon. Not. R. Astron. Soc. **493**, 3255 (2020).
[18] M. Ballardini, M. Braglia, F. Finelli, D. Paoletti, A. A. Starobinsky, and C. Umiltà, Scalar-tensor theories of gravity, neutrino physics, and the h_0 tension, J. Cosmol. Astropart. Phys. 10 (2020) 044.
[19] H. Hildebrandt, M. Viola, C. Heymans, S. Joudaki, K. Kuijken, C. Blake, T. Erben, B. Joachimi, D. Klaes, L. t. Miller *et al.*, Kids-450: Cosmological parameter constraints from tomographic weak gravitational lensing, Mon. Not. R. Astron. Soc. **465**, 1454 (2017).
[20] A. Leauthaud, S. Saito, S. Hilbert, A. Barreira, S. More, M. White, S. Alam, Behroozi, K. Bundy, J. Coupon *et al.*, Lensing is low: Cosmology, galaxy formation or new physics?, Mon. Not. R. Astron. Soc. **467**, 3024 (2017).
[21] W. Lin and M. Ishak, Cosmological discordances. ii. Hubble constant, planck and large-scale-structure data sets, Phys. Rev. D **96**, 083532 (2017).
[22] T. Abbott, F. Abdalla, A. Alarcon, J. Aleksić, S. Allam, S. Allen, A. Amara, J. Annis, J. Asorey, S. Avila *et al.*, Dark energy survey year 1 results: Cosmological constraints from galaxy clustering and weak lensing, Phys. Rev. D **98**, 043526 (2018).
[23] E. Di Valentino and S. Bridle, Exploring the tension between current cosmic microwave background and cosmic shear data, Symmetry **10**, 585 (2018).
[24] M. Asgari, T. Tröster, C. Heymans, H. Hildebrandt, J. L. v. d. Busch, A. H. Wright, A. Choi, T. Erben, B. Joachimi, S. Joudaki *et al.*, Kids+ viking-450 and des-y1 combined: Mitigating baryon feedback uncertainty with cosebis, Astron. Astrophys. **634**, A127 (2020).
[25] M. A. Buen-Abad, G. Marques-Tavares, and M. Schmaltz, Non-abelian dark matter and dark radiation, Phys. Rev. D **92**, 023531 (2015).
[26] R. Murgia, S. Gariazzo, and N. Fornengo, Constraints on the coupling between dark energy and dark matter from cmb data, J. Cosmol. Astropart. Phys. 04 (2016) 014.
[27] E. Di Valentino, C. Bœhm, E. Hivon, and F. R. Bouchet, Reducing the h 0 and σ8 tensions with dark matter-neutrino interactions, Phys. Rev. D **97**, 043513 (2018).
[28] J. C. Hill, E. McDonough, M. W. Toomey, and S. Alexander, Early dark energy does not restore cosmological concordance, Phys. Rev. D **102**, 043507 (2020).
[29] M. M. Ivanov, E. McDonough, J. C. Hill, M. Simonović, M. W. Toomey, S. Alexander, and M. Zaldarriaga, Constraining early dark energy with large-scale structure, Phys. Rev. D **102**, 103502 (2020).
[30] A. Klypin, V. Poulin, F. Prada, J. Primack, M. Kamionkowski, V. Avila-Reese, A. Rodriguez-Puebla, Behroozi, D. Hellinger, and T. L. Smith, Clustering and halo abundances in early dark energy cosmological models, arXiv:2006.14910.
[31] A. Doroshkevich, A. Klypin, and M. Khlopov, Large-scale structure of the universe in unstable dark matter models, Mon. Not. R. Astron. Soc. **239**, 923 (1989).
[32] M. Oguri, K. Takahashi, H. Ohno, and K. Kotake, Decaying cold dark matter and the evolution of the cluster abundance, Astrophys. J. **597**, 645 (2003).
[33] M.-Y. Wang and A. R. Zentner, Weak gravitational lensing as a method to constrain unstable dark matter, Phys. Rev. D **82**, 123507 (2010).
[34] M. Cirelli, E. Moulin, Panci, D. Serpico, and A. Viana, Gamma ray constraints on decaying dark matter, Phys. Rev. D **86**, 083506 (2012).
[35] M.-Y. Wang and A. R. Zentner, Effects of unstable dark matter on large-scale structure and constraints from future surveys, Phys. Rev. D **85**, 043514 (2012).
[36] O. E. Bjaelde, S. Das, and A. Moss, Origin of δneff as a result of an interaction between dark radiation and dark matter, J. Cosmol. Astropart. Phys. 10 (2012) 017.
[37] M.-Y. Wang, R. A. Croft, A. H. Peter, A. R. Zentner, and C. W. Purcell, Lyman-α forest constraints on decaying dark matter, Phys. Rev. D **88**, 123515 (2013).
[38] G. Blackadder and S. M. Koushiappas, Dark matter with two-and many-body decays and supernovae type ia, Phys. Rev. D **90**, 103527 (2014).
[39] S. Aoyama, T. Sekiguchi, K. Ichiki, and N. Sugiyama, Evolution of perturbations and cosmological constraints in decaying dark matter models with arbitrary decay mass products, J. Cosmol. Astropart. Phys. 07 (2014) 021.
[40] K. Enqvist, S. Nadathur, T. Sekiguchi, and T. Takahashi, Decaying dark matter and the tension in σ8, J. Cosmol. Astropart. Phys. 09 (2015) 067.
[41] V. Poulin, S. Pasquale, D., and L. Julien, A fresh look at linear cosmological constraints on a decaying dark matter component, J. Cosmol. Astropart. Phys. 08 (2016) 036.
[42] T. Bringmann, F. Kahlhoefer, K. Schmidt-Hoberg, and Walia, Converting nonrelativistic dark matter to radiation, Phys. Rev. D **98**, 023543 (2018).
[43] K. L. Pandey, T. Karwal, and S. Das, Alleviating the h0 and s8 anomalies with a decaying dark matter model, J. Cosmol. Astropart. Phys. 07 (2019) 026.

[44] K. Vattis, S. M. Koushiappas, and A. Loeb, Late universe decaying dark matter can relieve the h_0 tension, Phys. Rev. D **99**, 121302 (2019).

[45] M. Archidiacono, D. C. Hooper, R. Murgia, S. Bohr, J. Lesgourgues, and M. Viel, Constraining dark matter-dark radiation interactions with cmb, bao, and lyman-α, J. Cosmol. Astropart. Phys. 10 (2019) 055.

[46] S. J. Clark, K. Vattis, and S. M. Koushiappas, Cmb constraints on late-universe decaying dark matter as a solution to the h_0 tension, Phys. Rev. D **103**, 043014 (2021).

[47] B. S. Haridasu and M. Viel, Late-time decaying dark matter: Constraints and implications for the h_0-tension, Mon. Not. R. Astron. Soc. **497**, 1757 (2020).

[48] K. Enqvist, S. Nadathur, T. Sekiguchi, and T. Takahashi, Constraints on decaying dark matter from weak lensing and cluster counts, J. Cosmol. Astropart. Phys. 04 (2020) 015.

[49] S. Tulin and H.-B. Yu, Dark matter self-interactions and small scale structure, Phys. Rep. **730**, 1 (2018).

[50] M. Valli and H.-B. Yu, Dark matter self-interactions from the internal dynamics of dwarf spheroidals, Nat. Astron. **2**, 907 (2018).

[51] J. S. Bullock and M. Boylan-Kolchin, Small-scale challenges to the λcdm paradigm, Annu. Rev. Astron. Astrophys. **55**, 343 (2017).

[52] S. Aiola, A. Kosowsky, and B. Wang, Gaussian approximation of peak values in the integrated Sachs-Wolfe effect, Phys. Rev. D **91**, 043510 (2015).

[53] A. Kovács, C. Sánchez, J. García-Bellido, J. Elvin-Poole, N. Hamaus, V. Miranda, S. Nadathur, T. Abbott, F. Abdalla, J. Annis *et al.*, More out of less: An excess integrated Sachs–Wolfe signal from supervoids mapped out by the dark energy survey, Mon. Not. R. Astron. Soc. **484**, 5267 (2019).

[54] M. Aguilar, L. A. Cavasonza, B. Alpat, G. Ambrosi, L. Arruda, N. Attig, Azzarello, A. Bachlechner, F. Barao, A. Barrau *et al.*, Towards Understanding the Origin of Cosmic-Ray Electrons, Phys. Rev. Lett. **122**, 101101 (2019).

[55] A. Boyarsky, O. Ruchayskiy, D. Iakubovskyi, and J. Franse, Unidentified Line in X-Ray Spectra of the Andromeda Galaxy and Perseus Galaxy Cluster, Phys. Rev. Lett. **113**, 251301 (2014).

[56] M.-Y. Wang, A. H. Peter, L. E. Strigari, A. R. Zentner, B. Arant, S. Garrison-Kimmel, and M. Rocha, Cosmological simulations of decaying dark matter: Implications for small-scale structure of dark matter haloes, Mon. Not. R. Astron. Soc. **445**, 614 (2014).

[57] K. N. Abazajian, Sterile neutrinos in cosmology, Phys. Rep. **711**, 1 (2017).

[58] Y. Farzan and M. Rajaee, Dark matter decaying into millicharged particles as a solution to ams-02 positron excess, J. Cosmol. Astropart. Phys. 04 (2019) 040.

[59] A. Das, B. Dasgupta, and A. Ray, Galactic positron excess from selectively enhanced dark matter annihilation, Phys. Rev. D **101**, 063014 (2020).

[60] K. Ishiwata, O. Macias, S. Ando, and M. Arimoto, Probing heavy dark matter decays with multi-messenger astrophysical data, J. Cosmol. Astropart. Phys. 01 (2020) 003.

[61] C. Dessert, N. L. Rodd, and B. R. Safdi, The dark matter interpretation of the 3.5-kev line is inconsistent with blank-sky observations, Science **367**, 1465 (2020).

[62] S. Bhargava, Giles, A. Romer, T. Jeltema, J. Mayers, A. Bermeo, M. Hilton, R. Wilkinson, C. Vergara, C. Collins *et al.*, The xmm cluster survey: New evidence for the 3.5 kev feature in clusters is inconsistent with a dark matter origin, Mon. Not. R. Astron. Soc. **497**, 656 (2020).

[63] M.-Y. Wang, L. E. Strigari, M. R. Lovell, C. S. Frenk, and A. R. Zentner, Mass assembly history and infall time of the Fornax dwarf spheroidal galaxy, Mon. Not. R. Astron. Soc. **457**, 4248 (2016).

[64] M. Pospelov and M. Trott, R-parity preserving super-wimp decays, J. High Energy Phys. 04 (2009) 044.

[65] R. Allahverdi, B. Dutta, F. S. Queiroz, L. E. Strigari, and M.-Y. Wang, Dark matter from late invisible decays to and of gravitinos, Phys. Rev. D **91**, 055033 (2015).

[66] U. Ellwanger, H. Cyril, and M. T. Ana, The next-to-minimal supersymmetric standard model, Phys. Rep. **496**, 1 (2010).

[67] T. Higaki and F. Takahashi, Dark radiation and dark matter in large volume compactifications, J. High Energy Phys. 11 (2012) 125.

[68] J. D. Bowman, A. E. Rogers, R. A. Monsalve, T. J. Mozdzen, and N. Mahesh, An absorption profile centred at 78 megahertz in the sky-averaged spectrum, Nature (London) **555**, 67 (2018).

[69] K. Bondarenko, J. Pradler, and A. Sokolenko, Constraining dark photons and their connection to 21 cm cosmology with cmb data, Phys. Lett. B **805**, 135420 (2020).

[70] C. Bernard, K. Florian, and S. Marit, Primordial black holes as dark matter., Phys. Rev. D **94**, 085007 (2016).

[71] M. Raidal, V. Vaskonen, and H. Veermäe, Gravitational waves from primordial black hole mergers, J. Cosmol. Astropart. Phys. 09 (2017) 037.

[72] I. Masina, Dark matter and dark radiation from evaporating primordial black holes, Eur. Phys. J. Plus **135**, 552 (2020).

[73] R. Laha, Primordial Black Holes as a Dark Matter Candidate Are Severely Constrained by the Galactic Center 511 kev γ-Ray Line, Phys. Rev. Lett. **123**, 251101 (2019).

[74] S. Clesse and J. García-Bellido, Seven hints for primordial black hole dark matter, Phys. Dark Universe **22**, 137 (2018).

[75] Montero-Camacho, X. Fang, G. Vasquez, M. Silva, and C. M. Hirata, Revisiting constraints on asteroid-mass primordial black holes as dark matter candidates, J. Cosmol. Astropart. Phys. 08 (2019) 031.

[76] N. Smyth, S. Profumo, S. English, T. Jeltema, K. McKinnon, and Guhathakurta, Updated constraints on asteroid-mass primordial black holes as dark matter, Phys. Rev. D **101**, 063005 (2020).

[77] D. Jones, D. Scolnic, A. Riess, A. Rest, R. Kirshner, E. Berger, R. Kessler, Y.-C. Pan, R. Foley, R. Chornock *et al.*, Measuring dark energy properties with photometrically classified pan-starrs supernovae. ii. cosmological parameters, Astrophys. J. **857**, 51 (2018).

[78] S. Alam, M. Ata, S. Bailey, F. Beutler, D. Bizyaev, J. A. Blazek, A. S. Bolton, J. R. Brownstein, A. Burden,

C.-H. Chuang et al., The clustering of galaxies in the completed sdss-iii baryon oscillation spectroscopic survey: Cosmological analysis of the dr12 galaxy sample, Mon. Not. R. Astron. Soc. **470**, 2617 (2017).
[79] A. J. Ross, L. Samushia, C. Howlett, W. J. Percival, A. Burden, and M. Manera, The clustering of the sdss dr7 main galaxy sample–i. a 4 per cent distance measure at $z = 0.15$, Mon. Not. R. Astron. Soc. **449**, 835 (2015).
[80] F. Beutler, C. Blake, M. Colless, D. H. Jones, L. Staveley-Smith, G. B. Poole, L. Campbell, Q. Parker, W. Saunders, and F. Watson, The 6df galaxy survey: $z = 0$ measurements of the growth rate and σ_8, Mon. Not. R. Astron. Soc. **423**, 3430 (2012).
[81] J. Jin and Z. S. Jjie, *Computation of Special Functions* (Wiley, New York, 1996).
[82] C. Howlett, A. Lewis, A. Hall, and A. Challinor, Cmb power spectrum parameter degeneracies in the era of precision cosmology, J. Cosmol. Astropart. Phys. 04 (2012) 027.
[83] C.-Ma and E. Bertschinger, Cosmological perturbation theory in the synchronous and conformal newtonian gauges, Astrophys. J. **455**, 7 (1995).
[84] A. Lewis, Camb notes, 2011.
[85] K. Ichiki, M. Oguri, and K. Takahashi, Constraints from the Wilkinson Microwave Anisotropy Probe on Decaying Cold Dark Matter, Phys. Rev. Lett. **93**, 071302 (2004).
[86] D. Blas, J. Lesgourgues, and T. Tram, The cosmic linear anisotropy solving system (class). Part ii: Approximation schemes, J. Cosmol. Astropart. Phys. 07 (2011) 034.
[87] B. Audren, J. Lesgourgues, G. Mangano, D. Serpico, and T. Tram, Strongest model-independent bound on the lifetime of dark matter, J. Cosmol. Astropart. Phys. 12 (2014) 028.
[88] K. Heitmann, M. White, C. Wagner, S. Habib, and D. Higdon, The coyote universe. i. Precision determination of the nonlinear matter power spectrum, Astrophys. J. **715**, 104 (2010).
[89] J. Schaye, C. D. Vecchia, C. Booth, R. Wiersma, T. Theuns, M. R. Haas, S. Bertone, A. R. Duffy, I. McCarthy, and F. van de Voort, The physics driving the cosmic star formation history, Mon. Not. R. Astron. Soc. **402**, 1536 (2010).
[90] S. McAlpine, J. C. Helly, M. Schaller, J. W. Trayford, Y. Qu, M. Furlong, R. G. Bower, R. A. Crain, J. Schaye, T. Theuns et al., The eagle simulations of galaxy formation: Public release of halo and galaxy catalogues, Astron. Comput. **15**, 72 (2016).
[91] R. E. Smith, J. A. Peacock, A. Jenkins, S. D. M. White, C. S. Frenk, F. R. Pearce, A. Thomas, G. Efstathiou, and H. M. Couchmann, Stable clustering, the halo model and nonlinear cosmological power spectra, Mon. Not. R. Astron. Soc. **341**, 1311 (2003).
[92] S. Bird, M. Viel, and M. G. Haehnelt, Massive neutrinos and the non-linear matter power spectrum, Mon. Not. R. Astron. Soc. **420**, 2551 (2012).
[93] R. Takahashi, M. Sato, T. Nishimichi, A. Taruya, and M. Oguri, Revising the Halofit model for the nonlinear matter power spectrum, Astrophys. J. **761**, 152 (2012).
[94] A. Mead, C. Heymans, L. Lombriser, J. Peacock, O. Steele, and H. Winther, Accurate halo-model matter power spectra with dark energy, massive neutrinos and modified gravitational forces, Mon. Not. R. Astron. Soc. **459**, 1468 (2016).
[95] J. Dakin, S. Hannestad, and T. Tram, Fully relativistic treatment of decaying cold dark matter in n-body simulations, J. Cosmol. Astropart. Phys. 06 (2019) 032.
[96] M. Cataneo, L. Lombriser, C. Heymans, A. Mead, A. Barreira, S. Bose, and B. Li, On the road to percent accuracy: Non-linear reaction of the matter power spectrum to dark energy and modified gravity, Mon. Not. R. Astron. Soc. **488**, 2121 (2019).
[97] T. Abbott, F. Abdalla, S. Avila, M. Banerji, E. Baxter, K. Bechtol, M. Becker, E. Bertin, J. Blazek, S. Bridle et al., Dark energy survey year 1 results: Constraints on extended cosmological models from galaxy clustering and weak lensing, Phys. Rev. D **99**, 123505 (2019).
[98] A. R. Ade et al., Planck 2015 results. XIV. Dark energy and modified gravity, Astron. Astrophys. **594**, A14 (2016).
[99] H. Prince and J. Dunkley, Data compression in cosmology: A compressed likelihood for planck data, Phys. Rev. D **100**, 083502 (2019).
[100] J. Zuntz, M. Paterno, E. Jennings, D. Rudd, A. Manzotti, S. Dodelson, S. Bridle, S. Sehrish, and J. Kowalkowski, COSMOSIS: Modular cosmological parameter estimation, Astron. Comput. **12**, 45 (2015).
[101] S. Kumar, R. C. Nunes, and S. K. Yadav, Cosmological bounds on dark matter-photon coupling, Phys. Rev. D **98**, 043521 (2018).
[102] R. Cawthon, C. Davis, M. Gatti, Vielzeuf, J. Elvin-Poole, E. Rozo, J. Frieman, E. S. Rykoff, A. Alarcon, G. M. Bernstein et al., Dark energy survey year 1 results: Calibration of redmagic redshift distributions in des and sdss from cross-correlations, Mon. Not. R. Astron. Soc. **481**, 2427 (2018).
[103] E. S. Sheldon and E. M. Huff, Practical weak-lensing shear measurement with METACALIBRATION, Astrophys. J. **841**, 24 (2017).
[104] N. Aghanim, Y. Akrami, M. Ashdown, J. Aumont, C. Baccigalupi, M. Ballardini, A. Banday, R. Barreiro, N. Bartolo, S. Basak et al., Planck 2018 results. v. cmb power spectra and likelihoods, Astron. Astrophys. **641**, A5 (2020).
[105] A. Taruya, K. Koyama, T. Hiramatsu, and A. Oka, Beyond consistency test of gravity with redshift-space distortions at quasilinear scales, Phys. Rev. D **89**, 043509 (2014).
[106] A. Barreira, A. G. Sanchez, and F. Schmidt, Validating estimates of the growth rate of structure with modified gravity simulations, Phys. Rev. D **94**, 084022 (2016).
[107] W. Handley, M. Hobson, and A. Lasenby, POLYCHORD: Nested sampling for cosmology, Mon. Not. R. Astron. Soc.: Lett. **450**, L61 (2015).
[108] F. Feroz, M. Hobson, and M. Bridges, MULTINEST: An efficient and robust Bayesian inference tool for cosmology and particle physics, Mon. Not. R. Astron. Soc. **398**, 1601 (2009).
[109] G. Benevento, W. Hu, and M. Raveri, Can late dark energy transitions raise the Hubble constant?, Phys. Rev. D **101**, 103517 (2020).
[110] M. Raveri and W. Hu, Concordance and discordance in cosmology, Phys. Rev. D **99**, 043506 (2019).

[111] W. Handley and Lemos, Quantifying tension: Interpreting the des evidence ratio, Phys. Rev. D **100**, 043504 (2019).
[112] W. Wu, Motloch, W. Hu, and M. Raveri, Hubble constant tension between cmb lensing and bao measurements, Phys. Rev. D **102**, 023510 (2020).
[113] W. Handley, Anesthetic: Nested sampling visualisation, J. Open Source Softw. **4**, 1414 (2019).
[114] K. H. Knuth, M. Habeck, N. K. Malakar, A. M. Mubeen, and B. Placek, Bayesian evidence and model selection, Digit. Signal Process. **47**, 50 (2015).
[115] H. Jeffreys, *Theory of Probability* (Clarendon, Oxford, 1961).
[116] C. Robert, N. Chopin, J. Rousseau *et al.*, Harold Jeffreys's theory of probability revisited, Stat. Sci. **24**, 141 (2009).
[117] A. G. Riess, S. Casertano, W. Yuan, L. M. Macri, and D. Scolnic, Large magellanic cloud cepheid standards provide a 1% foundation for the determination of the Hubble constant and stronger evidence for physics beyond λcdm, Astrophys. J. **876**, 85 (2019).
[118] B. Giblin, M. Cataneo, B. Moews, and C. Heymans, On the road to per cent accuracy–ii. Calibration of the non-linear matter power spectrum for arbitrary cosmologies, Mon. Not. R. Astron. Soc. **490**, 4826 (2019).
[119] G. d'Amico, J. Gleyzes, N. Kokron, K. Markovic, L. Senatore, Zhang, F. Beutler, and H. Gil-Marín, The cosmological analysis of the sdss/boss data from the effective field theory of large-scale structure, J. Cosmol. Astropart. Phys. 05 (2020) 005.